Perforated closed-cell aluminium foam for acoustic absorption

KAMIL C. OPIELA[a]   TOMASZ G. ZIELIŃSKI[*a]   TOMÁŠ DVORÁK[b]   STANISLAV KÚDELA JR.[b]

[a]*Institute of Fundamental Technological Research, Polish Academy of Sciences, ul. Pawiński5B, 02-106 Warsaw, Poland*
[b]*Institute of Materials and Machine Mechanics, Slovak Academy of Sciences, Dúbravská cesta 9, 845 13 Bratislava, Slovakia*

Abstract

Closed-cell metal foams are lightweight and durable materials resistant to high temperature and harsh conditions, but due to their fully closed porosity they are poor airborne sound absorbers. In this paper a classic method of drilling is used for a nearly closed-cell aluminium foam to open its porous interior to the penetration of acoustic waves propagating in air, thereby increasing the wave energy dissipation inside the pores of the perforated medium. The aim is to investigate whether it is possible to effectively approximate wave propagation and attenuation in industrial perforated heterogeneous materials with originally closed porosity of irregular shape by means of their simplified microstructural representation based on computer tomography scans. The applied multi-scale modelling of sound absorption in foam samples is confronted with impedance tube measurements. Moreover, the collected numerical and experimental data is compared with the corresponding results obtained for perforated solid samples to demonstrate a great benefit coming from the presence of an initially closed porous structure in the foam.

Key words: Closed-cell metal foams; Perforation; Sound absorption; Microstructure effects; Dissipated powers

---

[*]*Corresponding Author*: tzielins@ippt.pan.pl

1   Introduction

Design and production of highly efficient noise absorbers and insulators that exhibit excellent low frequency properties while being lightweight and compact in size are still ongoing challenges. Various materials and their composites have been proposed so far to attenuate energy of acoustic waves: open-cell aluminium foams [1, 2], perforated closed-cell metal foams [3], ceramic foams with spherical pores [4], adaptable materials [5, 6], polymeric [7–11], composite [12], and double-porosity [13, 14] foams, polyurethane foams with thin membranes [15], syntactic hybrid foams (understood as open-cell polyurethane foams with embedded hollow micro-beads) [16], additively manufactured foams [17, 18], granular media [19–21], fibrous materials [22–24], micro-perforated plates with complex patterns of micro-slits [25, 26], porous composites like a polyurethane foam with sawdust [27] or a honeycomb sandwich panel [28], and even meta-porous [29, 30] as well as active [31] configurations. Among many possibilities, porous materials are considered a classic solution possessing very good sound absorption capabilities. It is essentially due to their specific internal structure composed of fluid-filled domains (i.e. pores) surrounded by solid walls (i.e. a skeleton). The energy of pressure waves penetrating them is effectively dissipated on the basis of thermal and visco-inertial effects [32], the intensity of which is directly related to the spatial distribution and geometry of pores. Thus, knowing the correspondence between the design and the relevant attributes of such media, it is possible to develop a particular configuration of a required acoustic behaviour. The fundamental prerequisite for the soundproofing to occur is the open nature of the porous structure, in other words, admission of penetration.

The propagation and suppression of airborne acoustic waves in open-cell foams have been research topics for many scientists until today. Therefore, such materials are quite well documented from this perspective in the literature. Perrot, Panneton, and Olny [1] (and a few years later De Jaeger, T'Joen, Huisseune, Ameel, and De Paepe [33]) conducted cellular morphology characterisation (idealised periodic unit cell reconstruction) of open-cell reticulated media and used their own method to accurately estimate two macroscopic parameters of utmost importance in sound absorbing materials. They and other authors also attempted to predict acoustical macro-behaviour of such or similar foams from the physics occurring on the local scale [34–36]. To accomplish that task for three commercially available porous metals, Otaru [36] made use of high-resolution computer tomography images. The influence of bulk density and static airflow resistivity of semi-open aluminium foams on their absorption properties was analysed in [37, 38]. In these works, pores were interconnected by small circular openings with sizes adjustable by varying the infiltration pressure. Moreover, Atalla, Panneton, Sgard, and Olny [39] as well as Sgard, Olny, Atalla, and Castel [40] revealed that a properly designed perforation can significantly enhance the acoustic performance of a mineral wool over a selected frequency band. Finally, purely experimental work on the determination of sound absorption coefficient for closed- (non-homogeneous, difficult to reproduce) and open-cell (of uniformly distributed and easily controllable pores) metal samples of the same thickness was reported in [41].

Rigid foams with closed porosity are usually poor acoustic absorbers, but good airborne noise insulators [42]. To reverse these intrinsic features, one needs to facilitate the penetration of acoustic waves in them. There typically exist three main strategies to open the porous network in materials of this type, namely (i) by a rolling (or compression) treatment that enables fracturing of many solid walls; (ii) by removing membranes between pores in consequence of a so-called reticulation process involving either thermal or chemical reactions; or (iii) through a (most efficient) hole drilling (perforation) technique that impacts global porosity by local skeleton modifications [3, 43–45]. Sound absorptivity of compressed/rolled closed-cell metal foams has been a subject of consideration of a number of papers so far, originating in late 1980s (e.g. [45, 46]). The review book by Ashby, Evans, Fleck, Gibson, Hutchinson, and Wadley [43, Chapter 12] is a good reference point here, summarising to some extent the first achievements in this field. Among rather rare previous publications that deal with the utilisation of the perforated closed-porosity media in acoustics (e.g. [3, 45]), a particular attention should be paid to the contribution from Chevillotte, Perrot, and Panneton [3], where the authors investigated the link between noise attenuation performance and microgeometry of a perforated cellular material with closed spherical (regular) pores. They built up an approximate theoretical model based on two-dimensional numerical analyses run on a simplified shape of a perforated closed-cell metal foam, and proposed a rough three-dimensional (3D) conversion for it. The foam studied in their work has (initially separated) pores that are connected by cylindrical channels. Thus, it exhibits similar behaviour to a perforated rigid solid, although its sound absorptivity is modulated by its local geometry, or, more specifically, by the interaction between the perforation diameter and pore size [3]. The content of the present article extends beyond the prior findings by Chevillotte et al. [3] to show various modelling results obtained for (i) a fully *three-dimensional* and locally *heterogeneous* real foam microstructure with eminently irregular pore sizes and shapes; (ii) a representative real geometry reconstructed from *computer tomography scans*; and (iii) an idealised (approximative) *periodic unit cell* that characterises the foam morphology. All these predictions are confronted with the corresponding experiments. The proposed largely simplified approach of periodic representative element generation may constitute a fast alternative to the sophisticated algorithm addressed in [47] that controls plenty of fine scale skeleton features.

In this paper one finds a complete path that was followed to evaluate the acoustic performance and potential of a (nearly) closed-cell metal foam adjusted to be an efficient sound absorber by applying regular cylindrical perforation. The fabrication and some physical properties of the investigated porous material are discussed in Section 2, with particular emphasis on data collected from computer micro-tomography scans. The samples prepared for testing in an impedance tube are introduced in Section 3, where the experimental setup and examined configurations are also briefly described.

Section 4 gives explanations regarding the mathematical modelling used for predicting the acoustic absorption. Finally, the results of sound absorption obtained for the samples from measurements in a wide frequency range are interpreted and compared with pertinent analytical and numerical calculations in Section 5.

2   Closed-porosity aluminium foam

An aluminium foam sample with virtually closed porosity (Figure 1a), also known as the Alulight, was prepared for the purposes of this work at the Institute of Materials and Machine Mechanics in Bratislava, Slovakia. The powder metallurgy route was selected to manufacture it under pressure, with AlSi10 (being an alloy comprising 10 wt.% of Si and Al balanced) as the foamable precursor, and 0.8 wt.% of TiH_2 (titanium hydrid) as the blowing agent. This method is very well established and has already resulted in a number of publications, such as [48–57]. In it, a compacted (extruded, rolled or isostatically pressed) and almost pore-less mixture of metal powder and blowing agent is heated above the melting temperature of the metal. Then, the foaming agent releases gas that expands the compacted precursor into a porous structure [57]. The fabrication procedure is ended with a rapid cooldown to room temperature, during which the action of residual gas pressure within the pores and associated subsequent non-uniform skeleton shrinkage are primary mechanisms of surface defects or cracks creation on solid walls [51]. However, the technique generally provides flexibility for making products of various shapes (e.g. panels, rods) due to the presence of steel moulds [57]. Other possible approaches to the production of metal foams are discussed, i.a. in [43, Chapter 2].
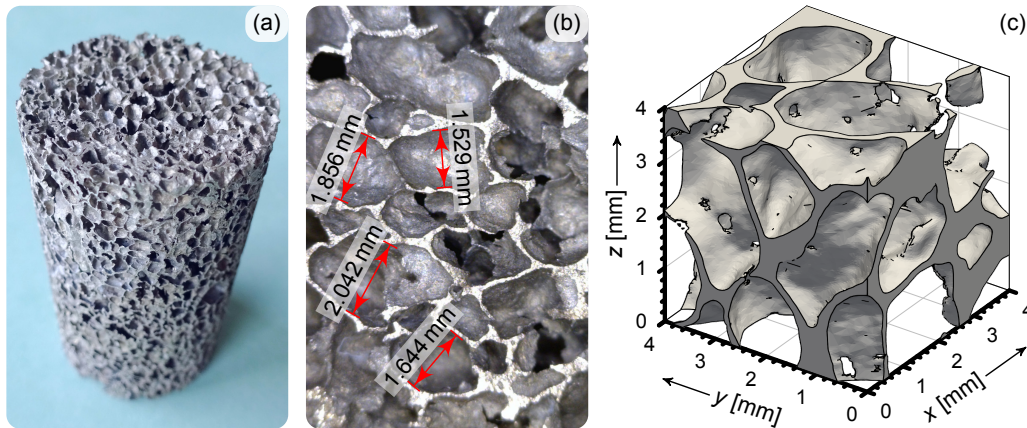

Figure 1: The aluminium foam sample under investigation: (a) general view (the top and lateral sides are visible); (b) enlarged view on the top of the sample (i.e. at height $z = 50\,\mathrm{mm}$); (c) typical microgeometry of the skeleton.

Controlling the process of creation of a closed porosity within a foam is not simple. In fact, the concept of fully closed pores is practically only theoretical. Aluminium shrinks during solidification which leads to the formation of micro-cracks in a skeleton. Therefore, nearly all pores are interconnected, although mostly by windows of very small dimensions, and moreover, there are in fact separate subnetworks of interconnected pores. All this results in a closed effective porosity of the foam samples. In the foam production process, the porosity can be influenced by varying the amount of TiH_2 in a semi-finished product, but only within a narrow interval. Alternatively, one can use the MgAl alloy to avoid the development of micro-cracks. The third possibility is to prepare a powder mixture of aluminium and other metals, which is then compacted and foamed. All in all, because the investigated Alulight foam is purely aluminium, one can say that the creation of closed pores in it is more or less random.

The cylindrical porous specimen of diameter $D \cong 29\,\mathrm{mm}$ and thickness $H_\mathrm{p} = 50\,\mathrm{mm}$ (Figure 1a) was cut out from a material panel using an electric discharge machine to ensure that it does not contain dense surface skin and is accurate. The following heat treatment was used to clean it after electric discharge cutting: heating of samples at rate $2\,^\circ\mathrm{C\,min^{-1}}$ followed by a one-hour dwell at $500\,^\circ\mathrm{C}$ and then cooling down to room temperature ($4\,^\circ\mathrm{C\,min^{-1}}$).

The obtained structure of the sample was verified under a microscope and with the help of GE Nanotom 180 computer tomography (CT) scans with the voxel size $0.03\,\mathrm{mm}$. Figure 1b presents a picture of the top surface of the specimen seen at certain magnification. When looking at it, one may observe that most of the pores have slightly oblate shape, are essentially closed and hardly linked with the adjacent air voids. Only a few have direct connections with other pores in the form of either a very tiny channels or narrow cracks on their walls (see also Figure 1c). As a result, at some distance from the incident surface the pore-fluid domain becomes dead-ended which strongly restricts acoustic wave propagation within the medium. From the point of view of sound penetration and absorption, the material can therefore be considered as having closed cellular microgeometry.

In addition to the microscopic survey, the computer analysis of CT pictures corresponding to particular sample cross-sections revealed that pores are mostly elongated in the axial direction or parallel to the horizontal base, with an average size of 1.7 mm (cf. [56]). From the 3D scan the sample porosity was calculated to be 0.8, whereas its measurements on
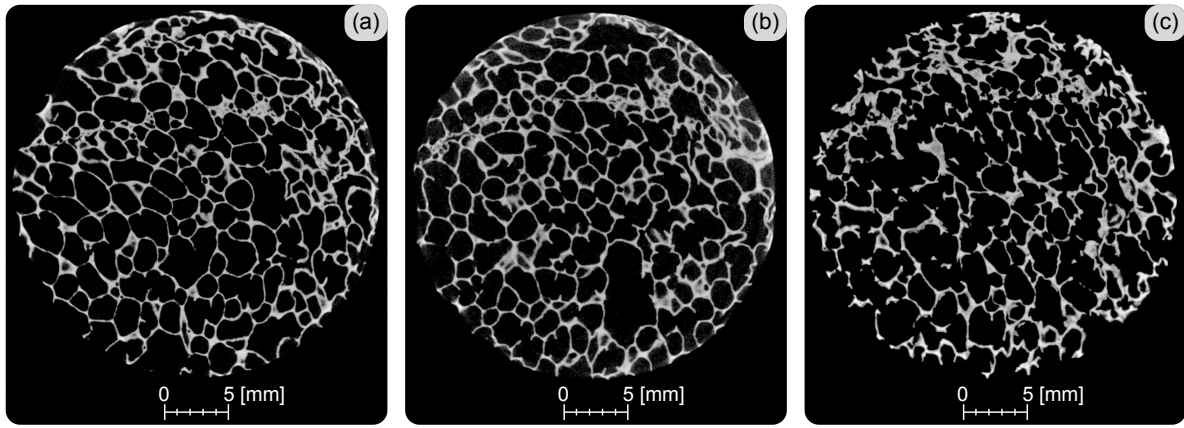
Figure 2: CT scan sections at different positions along the sample: (a) at height $z = 0$ mm (i.e. the bottom face of the sample); (b) at height $z = 36$ mm; (c) at height $z = 50$ mm (i.e. the top face of the sample).

the precise scales by a volumetric method (from the weight, density of the metal alloy equal $2650\,\text{kg/m}^3$, and geometry) gave the value of 0.83. Figure 2 illustrates the inner pore structure at certain positions along the sample axis. The z-locations of the three photographs shown in this figure were chosen to indicate key areas in the sample. The bottom (Figure 2a) and top (Figure 2c) of the specimen are nearly homogeneous when looking at the distribution and dimensions of void regions, although they may vary in terms of, for example, the distribution of intermetallic compounds in the cell wall aluminium [58]. On the other hand, there are places in the sample where individual pores are substantially larger than others in the vicinity. This case is emphasised in Figure 2b in its lower part where the metal skeleton locally vanishes, and is inherently caused by the chaotic nature of the foaming process [54]. Despite such technological inhomogeneities, the material can be treated as macroscopically isotropic due to high porosity (note that the degree of anisotropy of the foam usually decreases with increasing porosity) [49, 56, 57], which is controlled by the formation time [48, 52], temperature [48, 50], and the chemical composition of the substrates [55].

3 Preparation of samples for acoustic measurements

This section describes the macroscopic geometry of the investigated samples, as well as the measurement setup and the two configurations that were used to study absorption of airborne acoustic waves in closed-cell aluminium foams. The experimental data was acquired for the original foam and derivative materials with open porosities obtained by sequential perforation. Moreover, these results were compared not only with their numerical predictions, but also with the sound absorption obtained from measurements and analytically estimated for respective largely simplified geometries of perforated *solid* samples.

Seven metal foamed and polymer solid samples were prepared, each of them in the form of a cylinder with diameter $D \cong 29$ mm and height $H_\text{p} = 50$ mm. The porous and solid samples were perforated using a $d_\text{perf} = 2$ mm bit to reflect three regular patterns characterised by the distance l_perf between the axes of parallel holes, with l_perf equal to: (i) $l_1 = 16$ mm, (ii) $l_2 = 8$ mm, and (iii) $l_3 = 4$ mm, where numbers '1', '2', and '3' denote the particular pattern, from the rarest to the densest (see Figures 3a–3c). Such perforations in the case of solid samples led to the actual porosities of approximately: (i) $\phi_{\text{s},1} \approx 0.01$, (ii) $\phi_{\text{s},2} \approx 0.05$, (iii) $\phi_{\text{s},3} \approx 0.2$, respectively (here, the subscript 's' stands for 'solid'). The open porosities, ϕ, of the corresponding perforated foam samples were appropriately higher (the exact values are unknown, but, as it is expected, the denser the perforation, the bigger the deviation from the solid reference quantities) due to the opening of the initially closed pores in the original sample while the drilling process. Along with the three aforementioned patterns, the fourth *two-channel* regular perforation pattern having the same porosity as the third one but consisting of two cylindrical perforations per unit cell was proposed (see Figure 3d). Because it is characterised by the same distance l_perf as the third pattern, it is referred to as a pattern with $l_\text{perf} = l_{\text{tc},3} = l_3 = 4$ mm, where the subscript 'tc' is the acronym for 'two channels'. This pattern was used exclusively to numerically check whether the simpler pattern with $l_\text{perf} = l_3$ is dense enough to open the macroscopically closed initial foam microstructure, and to examine the effect of the perforation topology on the obtained results (cf. the graphs in Section 5). The value of d_perf was chosen to achieve nearly perfect absorption at the lowest possible frequencies. Following the analytical analysis made by Chevillotte et al. in [3] for perforated solids with porosity ϕ and thickness H, a specific perforation diameter d_perf^* that yields perfect sound absorption at the first peak can be predicted based on the power-law relation:

$$d_\text{perf}^*(\phi, H) = \zeta(\phi)\sqrt{H}, \tag{1}$$

with a certain coefficient $\zeta(\phi)$ which is geometry- and fluid-dependent. Assuming $\phi = \phi_{\text{s},2}$, $H = H_\text{p}$, dry air conditions, and rigid termination, one deduces $d_\text{perf}^* \approx 2$ mm (see Figure 6 in [3]). Taking $d_\text{perf} = d_\text{perf}^*$, l_perf must be equal to l_2 in order
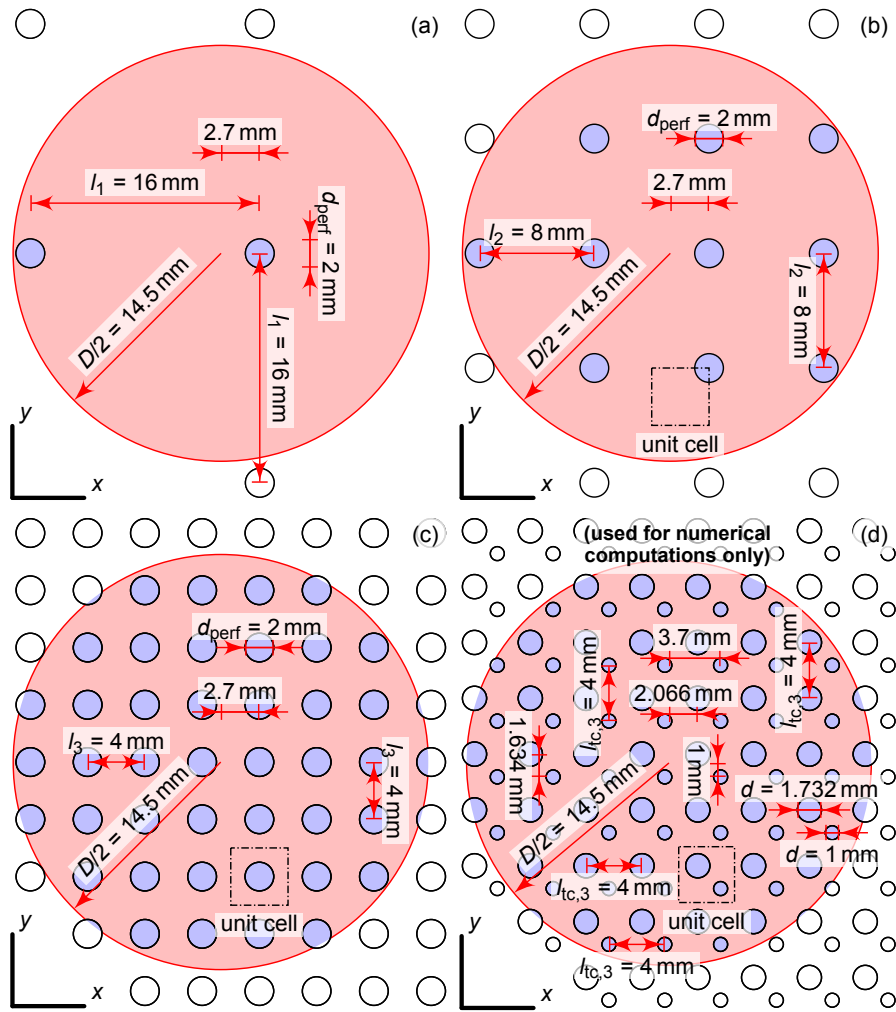
Figure 3: Perforation patterns and their dimensions: (a) pattern with $l_{\mathrm{perf}} = l_1$; (b) pattern with $l_{\mathrm{perf}} = l_2$; (c) pattern with $l_{\mathrm{perf}} = l_3$; (d) pattern with $l_{\mathrm{perf}} = l_{\mathrm{tc,3}}$. Red colour represents a sample, whereas the removed material is marked in blue. The dashed lines in (b, c, d) indicate the boundaries in the (x,y) plane of a cubic unit cell used in the numerical computations performed on the CT scanned metal foam microgeometry (see Figure 8).
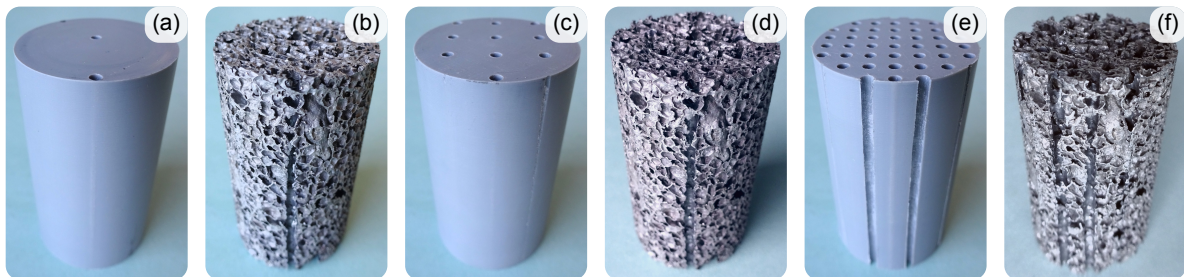

Figure 4: The manufactured perforated samples (the top and lateral sides are visible): solid samples (a, c, e) and aluminium foams (b, d, f) perforated applying the pattern with $l_{\mathrm{perf}} = l_1$ (a, b), $l_{\mathrm{perf}} = l_2$ (c, d), or $l_{\mathrm{perf}} = l_3$ (e, f).

to ensure the required porosity. The other three perforation patterns were obtained by doubling or halving the distance l_2 (see Figure 3).

The tested samples are presented in Figures 1a and 4. When the original foam sample was cut out from a material panel using an electric discharge machine, as already mentioned in Section 2, the polymer samples were individually fabricated from ABS (acrylonitrile butadiene styrene) filament in the Fused Deposition Modelling 3D printing technology [59] followed by a precise machining on a lathe of the top, bottom, and lateral surfaces to meet the desired dimensions. The perforation holes were either drilled on a computer numerical control milling machine in the case of the metal foams, or were broached in the polymer samples with an electric drill guided by additively manufactured channels of smaller diameter. Perfect circular shapes and good consistency with the designed characteristic sizes were confirmed by looking closely at the specimens under an optical microscope and by measuring their crucial dimensions. For example, some values determined for the solid sample with the third perforation pattern (for which $l_{\mathrm{perf}} = l_3$) are depicted in Figure 5.
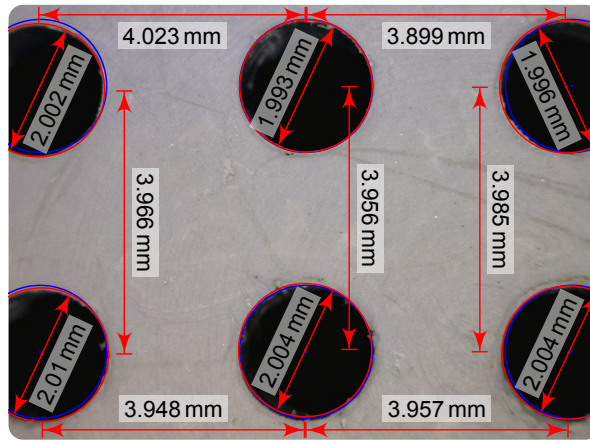
Figure 5: Microscopic measurements of actual dimensions (in red) for the perforated solid sample with $l_{\text{perf}} = l_3$ (top view) indicating deviations from the designed values and shapes (in blue).

Acoustic measurements were done in a 29-mm Brüel & Kjær impedance tube for frequencies ranging between $64\,\text{Hz}$ and $6400\,\text{Hz}$ ($500\,\text{Hz} - 6.4\,\text{kHz}$ is the nominal operational range for a tube of this diameter). The experiments were conducted in accordance with the Two-Microphone Transfer Function Method [60], in which the acoustic pressure is measured at two specific positions inside the tube. The correct operation of the instrumentation has recently been confirmed in a round robin study on acoustic testing of additively manufactured porous materials [61]. Based on the pressure levels and taking into account geometrical dimensions of the tube and physical properties of air, one evaluates the value of the sound absorption coefficient which is a frequency-dependent quantity varying from 0 (no attenuation) to 1 (perfect absorption). Two configurations were considered in the measurements: (i) with a sample directly backed by a rigid piston closing the impedance tube, and (ii) with an air gap of thickness $H_{\text{g}} = 10\,\text{mm}$ between the sample bottom and the rigid termination of the tube (in the latter case the total thickness of the porous layer and air gap was $60\,\text{mm}$). The metal specimens were additionally wrapped with thin tape (0.15 mm-thick) to protect the tube from scratches; after this action, all metal samples fitted very well to it.

4   Mathematical modelling used for sound absorption predictions

The experimental sound absorption curves were confronted with analytical and numerical predictions obtained using the equivalent-fluid approach for rigid-frame porous media [32]. The method relies on treating the investigated open-porosity material as a homogenised fluid that accurately reflects its macroscopic acoustic properties expressed in the equivalent density, $\varrho_{\text{e}}(\omega)$, and equivalent bulk modulus, $K_{\text{e}}(\omega)$, where $\omega \equiv 2\pi f$ is the wave angular frequency, f is the temporal frequency. These complex-valued equivalent quantities can be determined from the so-called dynamic visco-inertial, $\alpha(\omega)$, and dynamic thermal, $\alpha'(\omega)$, tortuosity functions, respectively, in conjunction with relevant parameters of the fluid saturating the space of open porosity ϕ, namely:

$$\varrho_{\text{e}}(\omega) = \frac{\varrho_{\text{air}}\alpha(\omega)}{\phi}\,, \qquad K_{\text{e}}(\omega) = \frac{K_{\text{air}}}{\phi\,\beta(\omega)} \quad \text{with} \quad \beta(\omega) = \gamma_{\text{air}} - \frac{\gamma_{\text{air}} - 1}{\alpha'(\omega)}\,. \tag{2}$$

The saturating fluid here is air, ϱ_{air} denotes its density, K_{air} is its bulk modulus, and γ_{air} is the ratio of specific heats (the adiabatic index) for air. Based on the assumption of plane wave fronts with normal incidence and using the equivalent properties (2), the Helmholtz equation of time-harmonic linear acoustics can be solved to describe the acoustic wave propagation in such dispersive media on the macroscale. Consequently, for a single hard-backed porous layer the surface acoustic impedance, $Z_{\text{s}}(\omega)$, is given by [32, 62]:

$$Z_{\text{s}}(\omega) = -\text{i}\,Z_{\text{e}}(\omega)\cot\left(\omega H_{\text{p}} c_{\text{e}}^{-1}(\omega)\right), \tag{3}$$

and for a two-layer system in which the porous material is backed by an air gap of thickness H_{g} before the rigid wall it is calculated as [32, 62]:

$$Z_{\text{s}}(\omega) = Z_{\text{e}}(\omega)\frac{Z_{\text{e}}(\omega) - \text{i}\,Z_{\text{g}}(\omega)\cot\left(\omega H_{\text{p}} c_{\text{e}}^{-1}(\omega)\right)}{Z_{\text{g}}(\omega) - \text{i}\,Z_{\text{e}}(\omega)\cot\left(\omega H_{\text{p}} c_{\text{e}}^{-1}(\omega)\right)}\,, \qquad Z_{\text{g}}(\omega) = -\text{i}\,Z_{\text{air}}\cot\left(\omega H_{\text{g}} c_{\text{air}}^{-1}\right). \tag{4}$$

In both expressions for the surface acoustic impedance, i.e. in Equations (3) and (4), i is the imaginary unit, $Z_{\text{e}}(\omega) = \sqrt{\varrho_{\text{e}}(\omega)K_{\text{e}}(\omega)}$ is the equivalent characteristic impedance, whereas $c_{\text{e}}(\omega) = \sqrt{K_{\text{e}}(\omega)/\varrho_{\text{e}}(\omega)}$ is the effective speed of sound in the equivalent medium. Knowing $Z_{\text{s}}(\omega)$ as well as the characteristic impedance, $Z_{\text{air}} = \sqrt{\varrho_{\text{air}}K_{\text{air}}}$, of the adjacent

fluid (which is the same as the fluid inside the pores and gap, i.e. air), the real-valued acoustic absorption coefficient, $\mathcal{A}(\omega)$, in the frequency range of interest can be determined from the formula [32, 62]:

$$\mathcal{A}(\omega) = 1 - \left| \frac{Z_{\mathrm{s}}(\omega) - Z_{\mathrm{air}}}{Z_{\mathrm{s}}(\omega) + Z_{\mathrm{air}}} \right|^2. \tag{5}$$

The sound absorptivity of the considered samples was modelled twofold: by means of theoretical and numerical analyses. The analytical approximations of the dynamic tortuosity functions, $\alpha_{\mathrm{A}}(\omega)$ and $\alpha'_{\mathrm{A}}(\omega)$, suitable for the perforated solid materials were computed from the expressions presented in Appendix A. This theoretical model requires only one geometrical parameter, d_{perf}, and three properties of air: μ_{air}, ϱ_{air}, and $N_{\mathrm{Pr,air}}$. Much more elaborate is a so-called hybrid multi-scale approach incorporating physical simulations conducted at the microstructure level. The numerical dynamic tortuosity functions, $\alpha_{\mathrm{N}}(\omega)$ and $\alpha'_{\mathrm{N}}(\omega)$, pertaining to all numerical solutions presented in Section 5, are estimated using the versatile Johnson-Champoux-Allard-Lafarge-Pride (JCALP) model of equivalent fluid valid for rigid-frame porous materials [32, 65–70]. It is essentially based on *eight* fluid-independent "transport" parameters, viz. the open porosity ϕ, (static) viscous permeability k_0, (static) thermal permeability k'_0, (high-frequency) tortuosity α_∞, static viscous tortuosity α_0, static thermal tortuosity α'_0, and two characteristic lengths: viscous Λ and thermal one Λ'. The subscripts '0' and '∞' here refer to 'static' quantities associated with $\omega = 0$, or to the high-frequency limit when $\omega \to \infty$, respectively. Appendix B provides the JCALP formulae and fundamental clarifications on how to work out the required transport parameters.

5   Results of acoustic measurements and modelling: comparison and discussion

Numerical analyses for the propagation along the thickness (height) of the cylindrical specimens were performed using the well-established finite element method [73, 74]. For the solid samples perforated with straight parallel channels, the three boundary value problems (see Appendix B) reduce to a single Poisson problem solved in two dimensions due to the geometrical invariance in the axial direction, as explained in detail in [26]. This is reflected in the identity between the corresponding viscous and thermal transport parameters, i.e. $\alpha_0 = \alpha'_0$, $k_0 = k'_0$, and $\Lambda = \Lambda'$. To better mirror the actual porosity of the manufactured solid specimens, the whole cross-section area of the cylindrical samples was used in calculations instead of just a unit cell. The fluid domains of the respective perforation patterns are indicated in blue in Figure 3.

The situation becomes more complicated for complex geometries, such as the one in Figure 1c, for which 3D numerical solutions to the Poisson, Laplace, and Stokes problems found inside the air domain are necessary to anticipate material acoustic properties by the multi-scale technique involving the JCALP model. Finite element computations were completed for a scanned cubic fragment with an edge length of $4\,\mathrm{mm}$ cut from the original porous microstructure. It was ensured that the cubic cell porosity, $\phi_{\mathrm{fc}} \approx 0.797$, and thermal characteristic length, $\Lambda'_{\mathrm{fc}} \approx 0.706\,\mathrm{mm}$, are very close to the reference values $\tilde{\phi}_{\mathrm{f}} \approx 0.799$ and $\Lambda'_{\mathrm{f}} \approx 0.7557\,\mathrm{mm}$, respectively, evaluated from CT images of a $12 \times 12 \times 24\,\mathrm{mm}$ interior part of the primary foam sample; the subscript 'f' here means 'foam', 'fc' is the abbreviation for 'foam cell', and $\tilde{\phi}$ denotes the total porosity, i.e. sum of the open and closed porosities. Furthermore, a convergence inspection of $\tilde{\phi}$ and Λ' with respect to the cubic cell size was conducted (see Figure 6), revealing the threshold edge length of the cell suitable for homogenisation at about 4 to 5 mm (much smaller than the shortest wavelength of interest). Therefore, it is assumed that the established unit cell was representative in further in-depth studies. In fact, a *periodic* unit cell would be more suitable here, if only a good periodic representation can be found for the chaotic (non-periodic) metal foam with a sufficiently regular microstructure to be considered quasi-periodic. Instead, the cube obtained from the CT scans would be an exact representation for an artificial foam composed of it and its mirrored copies forming together a periodic unit cell as shown in Figure 7a. Such a foam would have a periodic pore network that is fully open at the micro-scale level even before drilling. To better demonstrate the idea, the cubic cells and their mirrored copies were fabricated using additive manufacturing technology (see Figure 7b). However, for that purpose, the cell geometry had to be magnified (12.5 times) to accurately reproduce all its features using a device in Fused Deposition Modelling technology, and the aim of this work is to show that a mass-produced aluminium foam can be adapted (through the industrial perforation technique) to absorb sound, and not its 3D printed copy.

Simulations were also carried out for the same volume element with the second ($l_{\mathrm{perf}} = l_2$), third ($l_{\mathrm{perf}} = l_3$), and fourth ($l_{\mathrm{perf}} = l_{\mathrm{tc,3}}$) perforation patterns applied to it (see Figure 8), for which the porosity and thermal characteristic length increase to $\phi_{\mathrm{fc,2}} \approx 0.806$ and $\Lambda'_{\mathrm{fc,2}} \approx 0.745\,\mathrm{mm}$, $\phi_{\mathrm{fc,3}} \approx 0.835$ and $\Lambda'_{\mathrm{fc,3}} \approx 0.891\,\mathrm{mm}$, as well as $\phi_{\mathrm{fc,tc,3}} \approx 0.838$ and $\Lambda'_{\mathrm{fc,tc,3}} \approx 0.88\,\mathrm{mm}$, respectively. In all four cases, the symmetry was enforced on the fluid boundary faces in all three steady-state analyses, except for the boundaries normal to the z-axis, where the antisymmetry boundary condition was set in the Laplace and Stokes calculations [71].

In the next step, a periodic approximation of the extract of a rigid skeleton representative for the metal foam microgeometry (depicted in Figure 1c) was created using a random generation procedure. It consists of 50 spherical pores with
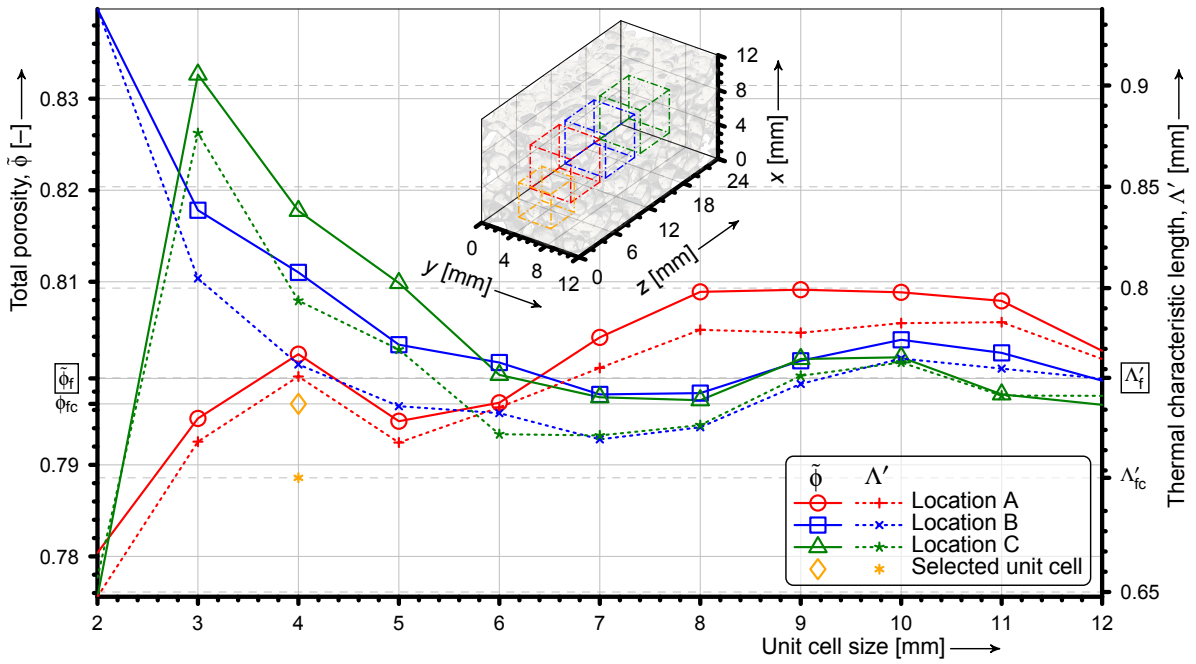
Figure 6: Convergence of the total porosity, $\tilde{\phi}$, and thermal characteristic length, Λ', as functions of the cubic unit cell size. The data was obtained for a series of unit cells centred in three different locations within the CT scanned real internal structure of the metal foam of dimensions $12 \times 12 \times 24$ mm: 'Location A'—at height $z = 6$ mm, 'Location B'—at height $z = 12$ mm, and 'Location C'—at height $z = 18$ mm along the axis of symmetry of the scanned fragment connecting points with coordinates $x = 6$ mm and $y = 6$ mm (middle line, not depicted). All locations of interest are shown graphically for unit cells of certain exemplary sizes, and the evaluated values are confronted with the parameters computed from the chosen unit cell (also drawn) as well as from the entire scanned region.
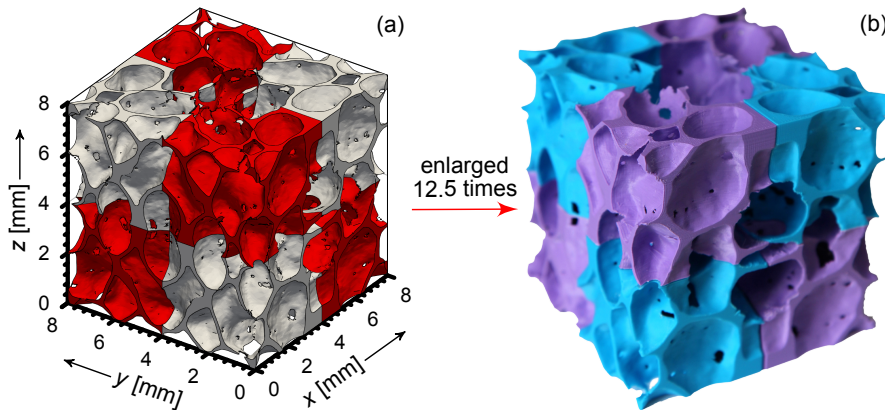
Figure 7: A periodic foam skeleton constructed from: (a) the scanned cubic $4 \times 4 \times 4$ mm fragments of the original porous microstructure (cf. Figure 1c), and their mirrored copies (marked in red); (b) the 3D printed scanned cubic fragments of the original porous microstructure enlarged 12.5 times (marked in cyan, cf. Figure 1c), and their mirrored copies (marked in violet).
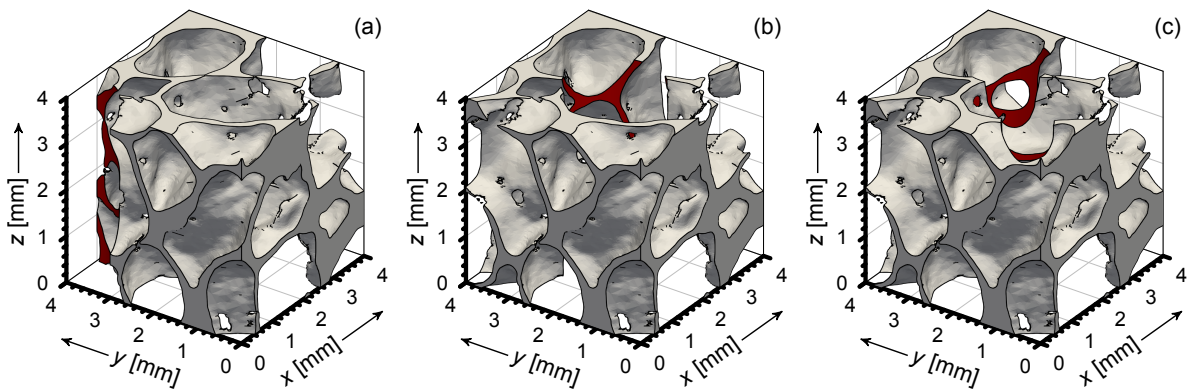

Figure 8: Perforated cell skeletons of the original metal foam: (a) with the second perforation pattern ($l_{\mathrm{perf}} = l_2$) applied to it; (b) with the third perforation pattern ($l_{\mathrm{perf}} = l_3$) applied to it; (c) with two cylindrical channels according to the fourth perforation pattern ($l_{\mathrm{perf}} = l_{\mathrm{tc},3}$). Perforation channels are marked in red.

radii varying between $0.24\,\text{mm}$ and $1.8\,\text{mm}$ (about $0.42\,\text{mm}$ in average) and has the open porosity $\phi_{ac} \approx 0.75$, while its thermal characteristic length is $\Lambda'_{ac} \approx 0.64\,\text{mm}$; here, the subscript 'ac' stands for 'approximate cell'. A simpler alternative of the algorithm described in [4] was utilised. It was essentially based on subtracting ideal spheres from the required cubic $4 \times 4 \times 4\,\text{mm}$ volume one by one. Pore positions and radii were selected so that the porosity and thermal length (which are taken directly from the shape of a unit cell, without solving any boundary value problem) are as close as possible to their target values (i.e. to $\tilde{\phi}_f$ and Λ'_f, respectively), while maintaining the mean size of pores as determined from microscopic measurements (see Figure 1b). During the generation process, attention was also paid to sequentially find spheres that penetrate with at least one another pore only by a small, predefined distance, or are not too far from the closest already drawn instance. Occasionally, little windows between pores were cut out or slightly enlarged by means of cylindrical surfaces. The size of the approximative periodic cell is $4\,\text{mm}$, which is also the size of the non-periodic unit cell selected from the scanned microgeometry, and, moreover, it is equal to the periodic interval $l_{perf} = l_3$ of the densest perforation pattern (see Figure 3c). In the second form of the periodic cell, a single perforation channel was added, which increases the porosity and thermal length so that $\phi_{ac,3} \approx 0.81$ and $\Lambda'_{ac,3} \approx 0.85\,\text{mm}$. The corresponding solid skeletons of both the periodic unit cell and its perforated variant are depicted in Figure 9.
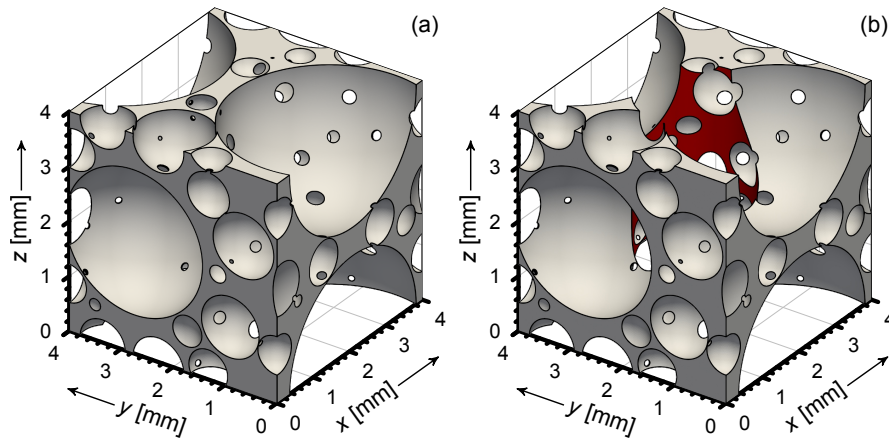

Figure 9: The periodic skeletons (unit cells) with pores of a spherical shape generated to approximate the aluminium foam: (a) the non-perforated cell; (b) the cell with a cylindrical channel (marked in red) realising the third perforation pattern with $l_{perf} = l_3$.

It is common that simplified periodic cellular designs are used in microstructure-based modelling (where periodicity is usually a must) to represent real non-periodic media. However, the proper construction of such designs is often difficult, and certainly not obvious nor unequivocal. Cells with randomly generated but periodic network of pores seem to be a good choice to represent a stochastic character of irregular media like the aluminium foam. Having a good periodic equivalent (at least in a wide range of frequencies) of a non-periodic material can be extremely useful for various research and re-design purposes. This is why an attempt to propose a random design of the periodic pore network that mimics the microstructure of the foam was made.

Exemplary results in terms of the Stokes velocity field scaled to the unit of permeability are shown in Figure 10. The flow through the original, non-perforated foam is considerably tortuous and has relatively low as well as rather uniform speed all over the fluid domain (Figure 10a). There are merely few places inside the cell where it is locally faster. This behaviour can be easily explained by a nearly closed nature of the primary porous network, with a small number of narrow windows that connect pores and enable deeper transport of air. The situation obviously changes when a cylindrical channel is drilled through the foam cell (see Figure 10b). Then, the maximum value of the scaled flow speed is increased by an order of magnitude. Furthermore, the streamlines are not so tortuous and pass mainly through the channel. More importantly, some of the initially poorly accessible pores are now fully open to flow. Very similar observations are made when analysing the viscous flow through the periodic cell that approximate the microstructure of the non-periodic aluminium foam. This is illustrated in Figure 10c and also in Figure 10d for the perforated periodic cell. The flow through the approximative cell is again very sinuous and directed to little linking necks, and it significantly changes once the perforation is applied. It should be noted that the typical values of the scaled velocity are similar or very similar to the corresponding values found for the original foam which confirms good match of a periodic approximation and the real microstructure.

The closed-cell aluminium foam sample and the three perforated polymer samples were tested for sound absorption in an impedance tube. Experiments were also made for the sequentially perforated metal specimen that had been already tested, starting from the first perforation pattern and then moving on to the second and the third ones by simply drilling additional channels (see Figures 3 and 4). During the measurements in the impedance tube, the samples were inserted with their tops facing the loudspeaker generating white noise. The lateral side of the metal samples was wrapped with thin tape to prevent the tube from being scratched. Two tests were carried out for each specimen, viz.: (i) for a sample directly backed by the rigid termination of the tube, and (ii) with a 10-mm air gap between the rigid backing and the bottom face of the sample.
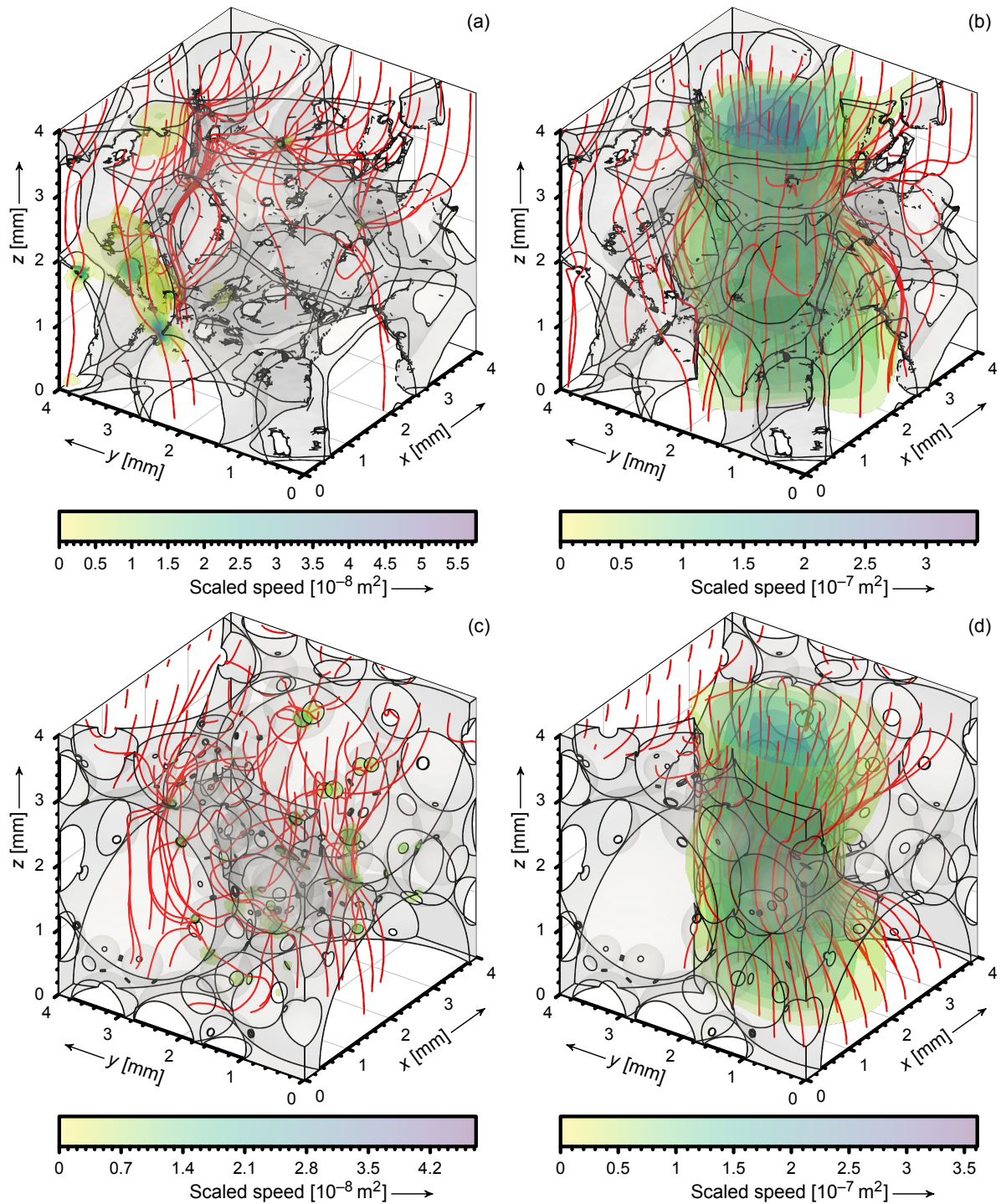
Figure 10: Viscous, incompressible flow through the porous unit cells of: (a, b) the real, non-periodic microgeometry, and (c, d) the approximative, periodic one. Two cases are considered for each microgeometry: (a, c) the non-perforated cells, and (b, d) the cells with a cylindrical channel along the z-axis, according to the third perforation pattern ($l_{\mathrm{perf}} = l_3$). Magnitude contours of the scaled velocity (isovalues as indicated by colour bar labels) as well as streamlines (red lines) are shown for the flows driven by the pressure gradient parallel to the z-axis (i.e. the macroscopic direction of wave propagation).

Figures 11, 12, and 13 present the normal incidence acoustic absorption obtained experimentally (and in the polymer sample case also computationally) for the first ($l_{\mathrm{perf}} = l_1$), second ($l_{\mathrm{perf}} = l_2$), and third ($l_{\mathrm{perf}} = l_3$) perforation pattern, respectively, applied to the metal as well as polymer samples. Figure 13 contains a numerical curve pertaining to the fourth perforation pattern ($l_{\mathrm{perf}} = l_{\mathrm{tc},3}$) realised on a polymer sample too. The values measured for the non-perforated metal foam in the two configurations (i.e. with and without an air gap) are included for comparison. Important observations are discussed below.

The original, non-perforated foam sample does have some open or partly-open pores (the values of the absorption coefficient are significantly higher than zero; see Figure 11, for instance), but only within a restricted area beginning at the incident face. It means that the acoustic wave cannot penetrate deeply inside the specimen and in particular does not reach
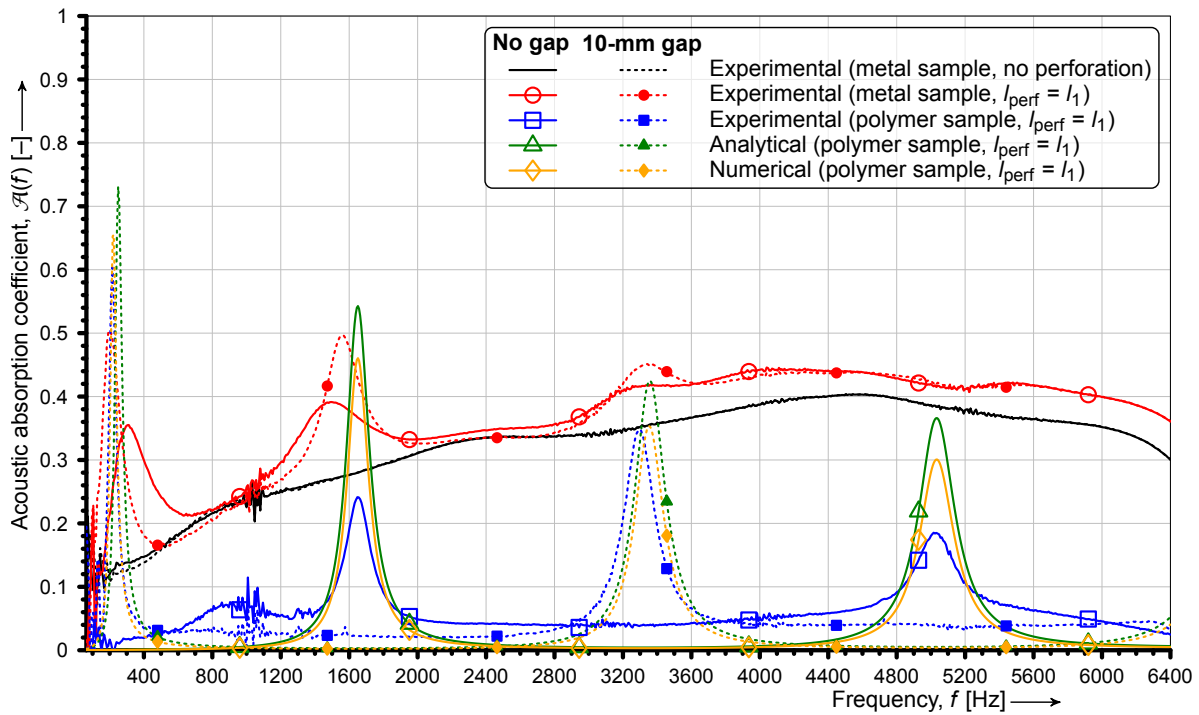
Figure 11: Sound absorption of samples with the first perforation pattern ($l_{\text{perf}} = l_1$).
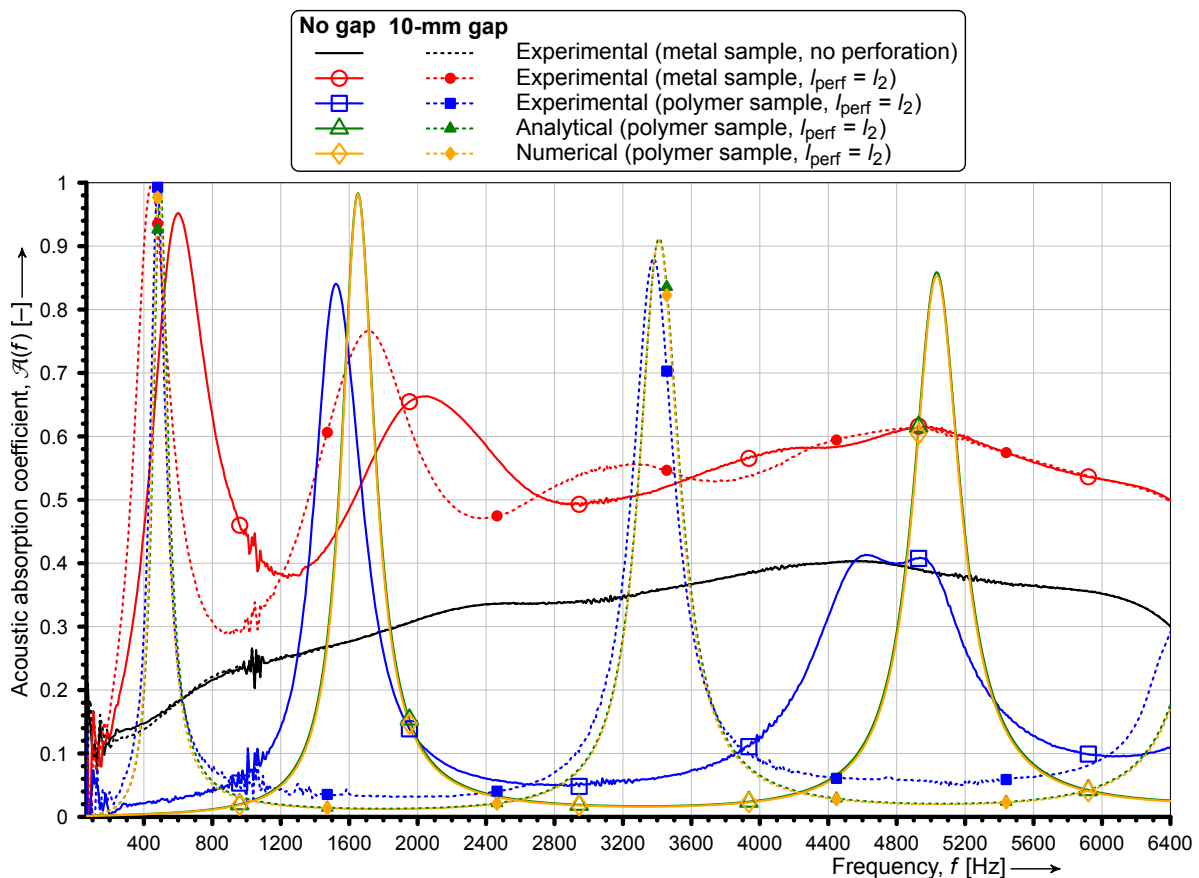

Figure 12: Sound absorption of samples with the second perforation pattern ($l_{\text{perf}} = l_2$).

the air gap behind it so that the presence of the gap has no effect on the absorption. Therefore, the overall ("effective") porosity in the non-perforated foam sample is undoubtedly closed from the macroscopic standpoint.

The analytical and numerical results incorporating the JCALP model are in perfect agreement except for the first perforation pattern (cf. Figure 11 with Figures 12 and 13). This is because in this case the perforation is poorly reflected in the sample due to relatively large distances between cylindrical channels, i.e. $l_{\text{perf}} = l_1 = 16\,\text{mm}$, while the diameter
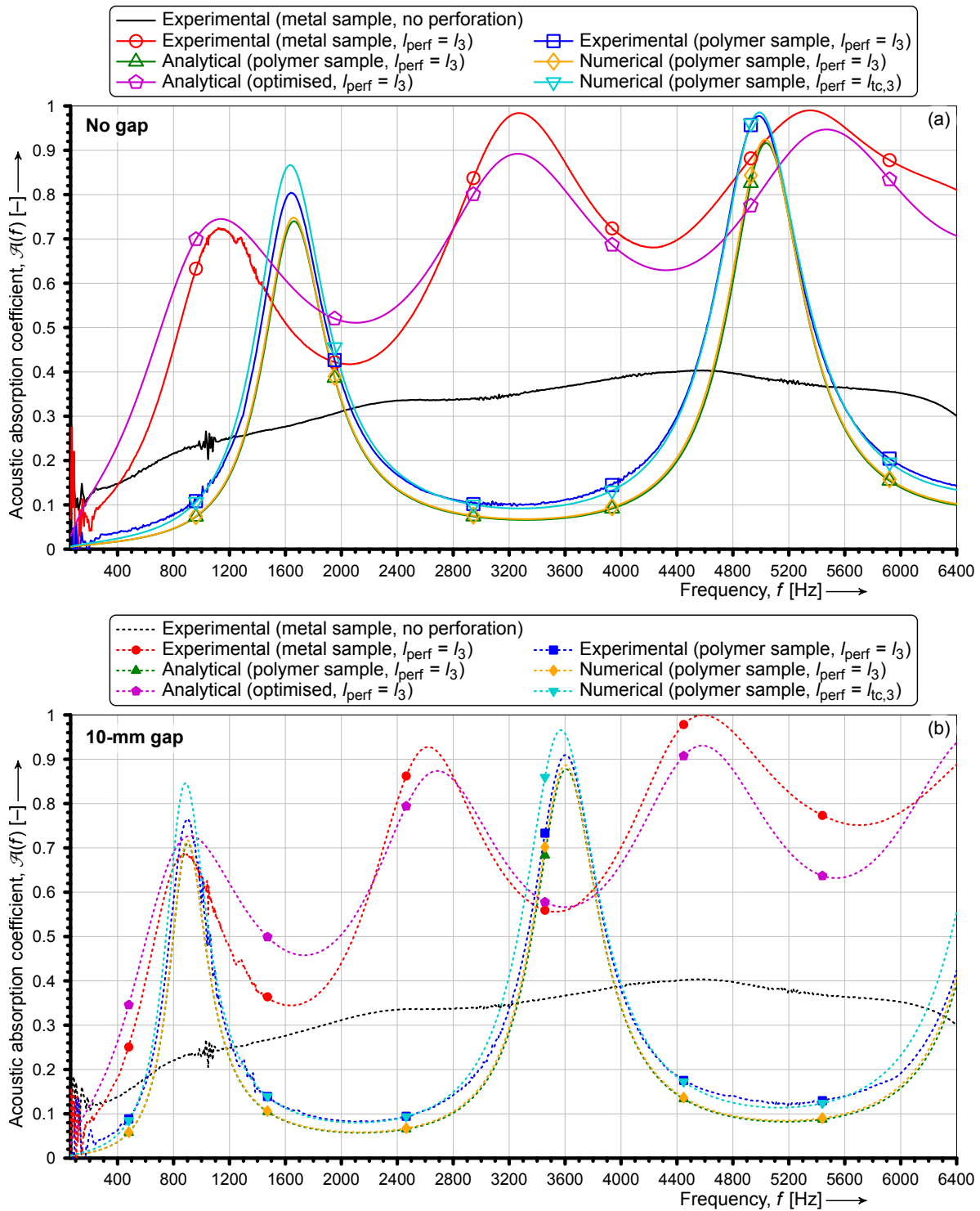
Figure 13: Sound absorption of samples with the third perforation pattern ($l_{\text{perf}} = l_3$): (a) without an air gap, and (b) with a 10-mm air gap between the material and rigid termination.

of the sample $D \cong 29$ mm is not even twice as large. In consequence, the transport parameters (even porosity) computed in the hybrid multi-scale method for the actual specimen are substantially different than the analogical set of parameters obtained for the sample of a diameter sufficiently large to capture the periodic character of the perforation. Hence, the analytical and numerical predictions use different porosity values and lead to non-overlapping curves (if the porosity in the analytical model is adjusted, the discrepancies are almost negligible).

The experimental absorption curves plotted for the perforated solid samples correspond well to the respective analytical and numerical estimations. In particular, the absorption peaks, as well as the very low level of absorption between them, are well reproduced in experiments, indicating good surface finish and generally high quality of the polymer specimens. Despite some differences which may be related to imperfections in manufacturing and testing, the experimental and calculated curves are in good qualitative accordance for both configurations, i.e. with and without the air gap behind

the samples. From a practical point of view, the frequencies of the quarter-wavelength resonance, which are related with peaks in absorption of hard-backed porous layers, are well assessed. The computations show that the application of the two-channel perforation of the fourth pattern ($l_{\text{perf}} = l_{\text{tc},3}$) should improve absorption of polymer samples in comparison with the third pattern with $l_{\text{perf}} = l_3$ and a single perforation channel, despite having virtually the same porosities.

The perforated aluminium foam specimens outperform their solid polymer counterparts in sound absorption. They are generally much better in a wide frequency range. Even for the case with no air gap behind the porous material, their first absorption peak (the quarter-wavelength layer resonance) is massively shifted to lower frequencies (about 1.1 kHz for $l_{\text{perf}} = l_3$, and below for $l_{\text{perf}} = l_1$ or $l_{\text{perf}} = l_2$) just because of the perforation that modified the microstructure. In some way the reported superior acoustic response is imitating the enhanced wave attenuation in narrow tubes with periodically spaced lateral dead-end cavities investigated in [75], and it comes from the decrease in sound speed understood as $\operatorname{Re} c_{\text{e}}(\omega)$. In crude terms, this statement is always true for all damping porous media saturated with air, in which $\operatorname{Re} c_{\text{e}}(\omega)$ is less than the speed of sound in the open air for any ω. Nonetheless, here it is caused by intensified viscous phenomena emerging from the opened side branches throughout the sample height on account of the perforation. A distinct gain also originate from the thermal effects occurring in the channels and pores adjacent to them. This hypothesis is confirmed by analysing the so-called time-averaged partial dissipated powers, as well as the corresponding partial acoustic absorption coefficients, pertaining to the artificial materials based either on the CT scanned foam cell (see Figure 1c) or its perforated variant.

The time-averaged power $\mathcal{P}(\omega)$ dissipated by airborne waves propagating in rigid-frame porous materials can be decomposed into its viscous $\mathcal{P}_{\text{vis}}(\omega)$ and thermal part $\mathcal{P}_{\text{th}}(\omega)$, i.e. $\mathcal{P}(\omega) = \mathcal{P}_{\text{vis}}(\omega) + \mathcal{P}_{\text{th}}(\omega)$. When the equivalent properties (2) are known and the field of acoustic pressure p is determined within the considered domain Ω_{p} of the porous medium, the partial dissipated powers can be calculated from the following formulae [39] (see also [76] for the dissipated energies in poroelastic media):

$$\mathcal{P}_{\text{vis}}(\omega) = -\frac{\operatorname{Im} \varrho_{\text{e}}(\omega)}{|\varrho_{\text{e}}(\omega)|^2} \frac{1}{2\omega} \int_{\Omega_{\text{p}}} |\nabla p(\omega)|^2 \, \mathrm{d}V \tag{6}$$

and

$$\mathcal{P}_{\text{th}}(\omega) = \frac{\operatorname{Im} K_{\text{e}}(\omega)}{|K_{\text{e}}(\omega)|^2} \frac{\omega}{2} \int_{\Omega_{\text{p}}} |p(\omega)|^2 \, \mathrm{d}V \,. \tag{7}$$

For plane incident acoustic waves propagating into a homogeneous porous layer with thickness H_{p} and backed at $z = 0$ mm by a rigid wall, analytical solutions are found for the acoustic pressure field and its gradient:

$$p(\omega; z) = p_{\text{s}} \frac{\cos\left(k_{\text{e}}(\omega)z\right)}{\cos\left(k_{\text{e}}(\omega)H_{\text{p}}\right)} \,, \qquad \nabla p(\omega; z) = p_{\text{s}} \frac{\mathrm{i}k_{\text{e}}(\omega)\sin\left(k_{\text{e}}(\omega)z\right)}{\cos\left(k_{\text{e}}(\omega)H_{\text{p}}\right)} \,, \tag{8}$$

where $z \in [0, H_{\text{p}}]$, p_{s} is the known, real-valued pressure amplitude applied at the layer surface (i.e. at $z = H_{\text{p}}$), and $k_{\text{e}}(\omega) = \omega \, c_{\text{e}}^{-1}(\omega)$ is the complex wavenumber in the equivalent material. Let $k_{\text{R}} \equiv \operatorname{Re} k_{\text{e}}$ and $k_{\text{I}} \equiv \operatorname{Im} k_{\text{e}}$ denote its real and imaginary part, respectively. Now, the integral in (7) can be expressed by the analytical formula:

$$\int_{\Omega_{\text{p}}} |p(\omega)|^2 \, \mathrm{d}V = S_{\text{p}} \int_0^{H_{\text{p}}} |p(\omega)|^2 \, \mathrm{d}z = \frac{p_{\text{s}}^2 S_{\text{p}}}{4} \frac{k_{\text{I}}^{-1}(\omega)\sinh\left(2k_{\text{I}}(\omega)H_{\text{p}}\right) + k_{\text{R}}^{-1}(\omega)\sin\left(2k_{\text{R}}(\omega)H_{\text{p}}\right)}{\sinh^2\left(k_{\text{I}}(\omega)H_{\text{p}}\right) + \cos^2\left(k_{\text{R}}(\omega)H_{\text{p}}\right)} \,, \tag{9}$$

while the integral in (6) as:

$$\int_{\Omega_{\text{p}}} |\nabla p(\omega)|^2 \, \mathrm{d}V = S_{\text{p}} \int_0^{H_{\text{p}}} |\nabla p(\omega)|^2 \, \mathrm{d}z$$

$$= \frac{p_{\text{s}}^2 S_{\text{p}}}{4} \left(k_{\text{R}}^2(\omega) + k_{\text{I}}^2(\omega)\right) \frac{k_{\text{I}}^{-1}(\omega)\sinh\left(2k_{\text{I}}(\omega)H_{\text{p}}\right) - k_{\text{R}}^{-1}(\omega)\sin\left(2k_{\text{R}}(\omega)H_{\text{p}}\right)}{\sinh^2\left(k_{\text{I}}(\omega)H_{\text{p}}\right) + \cos^2\left(k_{\text{R}}(\omega)H_{\text{p}}\right)} \,. \tag{10}$$

In both formulae, S_{p} is the face area of the considered part of the porous layer. For the cylindrical specimens: $\|\Omega_{\text{p}}\| = S_{\text{p}} H_{\text{p}}$ and $S_{\text{p}} = \frac{\pi}{4} D^2$.

The partial dissipated powers can be used to decompose the (total) sound absorption coefficient $\mathcal{A}(\omega)$ into its viscous $\mathcal{A}_{\text{vis}}(\omega)$ and thermal part $\mathcal{A}_{\text{th}}(\omega)$ in the same way as it was done in [76] using the dissipation energies in poroelastic media. In the case of rigid porous materials, $\mathcal{A}(\omega) = \mathcal{A}_{\text{vis}}(\omega) + \mathcal{A}_{\text{th}}(\omega)$, where

$$\mathcal{A}_{\text{vis}}(\omega) = \frac{\mathcal{P}_{\text{vis}}(\omega)}{\mathcal{P}(\omega)} \mathcal{A}(\omega) \,, \qquad \mathcal{A}_{\text{th}}(\omega) = \frac{\mathcal{P}_{\text{th}}(\omega)}{\mathcal{P}(\omega)} \mathcal{A}(\omega) \,. \tag{11}$$

Figure 14a presents the dissipated powers computed for the artificial materials based either on the CT scanned foam cell (see Figure 1c) or its perforated variant ($l_{\text{perf}} = l_3$), and normalised (divided) by the same reference power $\mathcal{P}_{\text{ref}}$,

calculated as the total power dissipated at the lowest audible frequency, for which the energy dissipation is very low, when there is no perforation, viz. $\mathcal{P}_{\mathrm{ref}} \equiv \mathcal{P}\left(2\pi f_{\mathrm{ref}}\right)$ with $f_{\mathrm{ref}} = 20\,\mathrm{Hz}$. Because of the applied normalisation, the terms $p_{\mathrm{s}}^2 S_{\mathrm{p}}$ in Equations (9) and (10) cancel out so that the results are independent on the excitation pressure and the waveguide cross-section. The values of the total and corresponding partial absorption coefficients are plotted in Figure 14b, where they are also confronted with the (total) sound absorption measured for the aluminium foam sample with and without perforation.
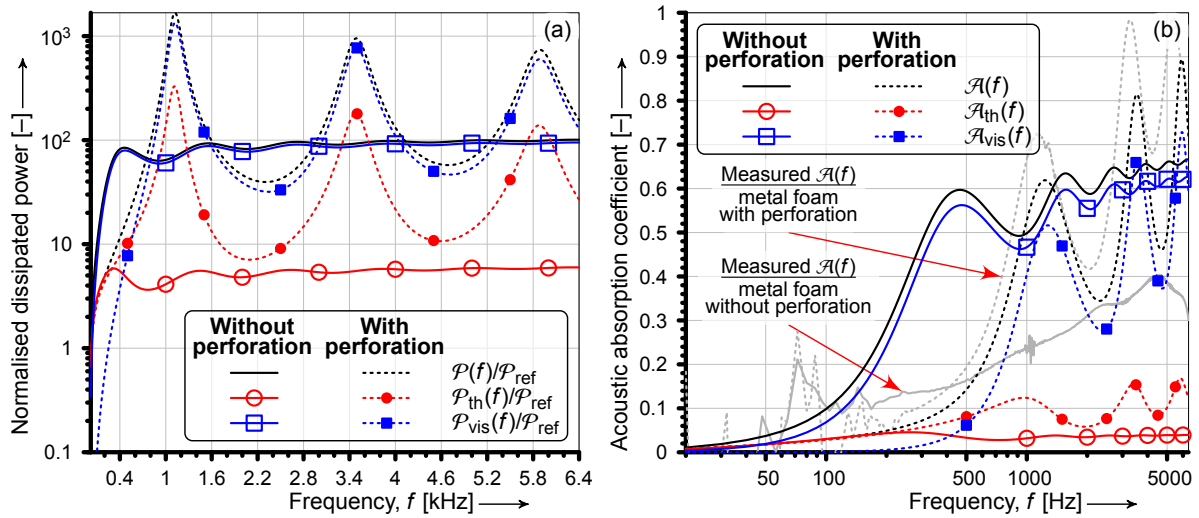
Figure 14: Components of the acoustic wave energy dissipation (predicted using the unit cells depicted in Figures 1c and 8b) within the metal foam sample (no air gap) without perforation or with perforation ($l_{\mathrm{perf}} = l_3$) due to thermal and viscous effects: (a) time-averaged dissipated total and partial powers normalised by the reference total power, $\mathcal{P}_{\mathrm{ref}}$, calculated at the lowest frequency in the audible spectrum, $f_{\mathrm{ref}} = 20\,\mathrm{Hz}$, for the non-perforated case; (b) contributions of the various mechanisms in the total sound absorption.

The contributions of the partial powers and absorption coefficients to their respective total quantities (see Figure 14) show that the characteristic frequency at which the viscous interaction between air and the solid skeleton becomes the major mechanism of energy dissipation is moved from $47\,\mathrm{Hz}$ to about $572\,\mathrm{Hz}$ as long as the metal foam is perforated with $l_{\mathrm{perf}} = l_3$ (see Figure 14b). At the same time, the importance of thermal losses grows on average by $270\,\%$ in the whole frequency range of interest. As a matter of fact, the tortuosity is largely decreased in the sample composed of the CT scanned cells with the central cylindrical channel in consequence of the perforation (as it is for the real metal specimens too), but the drop can be made smaller by, for example, drilling inclined and narrower holes instead of the proposed ones. Despite this drawback, the perforation allows the acoustic wave to propagate in the greater volume of the pore-fluid and to reach the air cavity at the back, which were the fundamental reasons for applying it. What should be emphasised here, however, is that the results presented in Figure 14 were obtained for non-existing materials of fully open porosity that had been created from the relevant cubic representative cell replicated in three mutually perpendicular directions to yield the same thickness as the primary metal foam specimen has. Their dissipative properties, in turn, serve only to demonstrate the relevance and the induced change of the individual mechanisms taking place at the macroscale level. Moreover, one should note that the predicted (total) absorption values are close to the experimental data when the perforation is considered, otherwise, as expected, they do not agree with measurements at all (cf. Figures 14b and 15). This suggests that the speculation on the composition of the resulting foam microgeometry including definitely more open than dead-end porosity is legitimate.

The porous structure of the aluminium samples has a great impact on the augmentation of sound energy dissipation within the perforated foams. Curve-fitting studies involving parametric optimisation (to minimise the difference between the analytical and experimental curves) that were carried out for the porous specimen with the third perforation pattern ($l_{\mathrm{perf}} = l_3$) in the configuration without an air gap reveal that to obtain comparable absorption characteristics, a solid (i.e. initially *not* porous) material needs to have cylindrical perforation 2.52 times smaller in diameter (i.e. $0.8\,\mathrm{mm}$) and distributed 4.64 times denser (that is to say, every $0.86\,\mathrm{mm}$ with $\phi_{\mathrm{s},3} \approx 0.67$) while increasing the thickness of the medium by a factor of 1.5 (to $74.8\,\mathrm{mm}$). For the case with an air gap between the sample and rigid termination, the conclusions are very similar: the foam behaves like an analogous solid material with perforation diameter $0.89\,\mathrm{mm}$ (2.25 times smaller), perforation spacing $0.99\,\mathrm{mm}$ (almost 4.06 times smaller), porous layer thickness $77.8\,\mathrm{mm}$ (1.56 times bigger), and air gap thickness $9.4\,\mathrm{mm}$ (1.06 times smaller), leading to the porosity equal approximately 0.64. Such perforated absorber, when made of aluminium, would be 2.2 times heavier than the perforated foam with a porosity of 0.835. The corresponding two plots are shown in Figure 13.

More results of the modelling of sound propagation in the metal porous specimens are juxtaposed in Figures 15–17. They actually disclose many difficulties in mimicking the complex behaviour of a real isotropic foam of this sort. The numerical curves describing the non-perforated sample (both CT- and approximation-based) are similar and follow the steady character of their experimental counterpart, but also show much higher absorption and differ in the presence of the air gap, which means that the porosities of the relevant specimens are not sufficiently closed, in other words, their flow
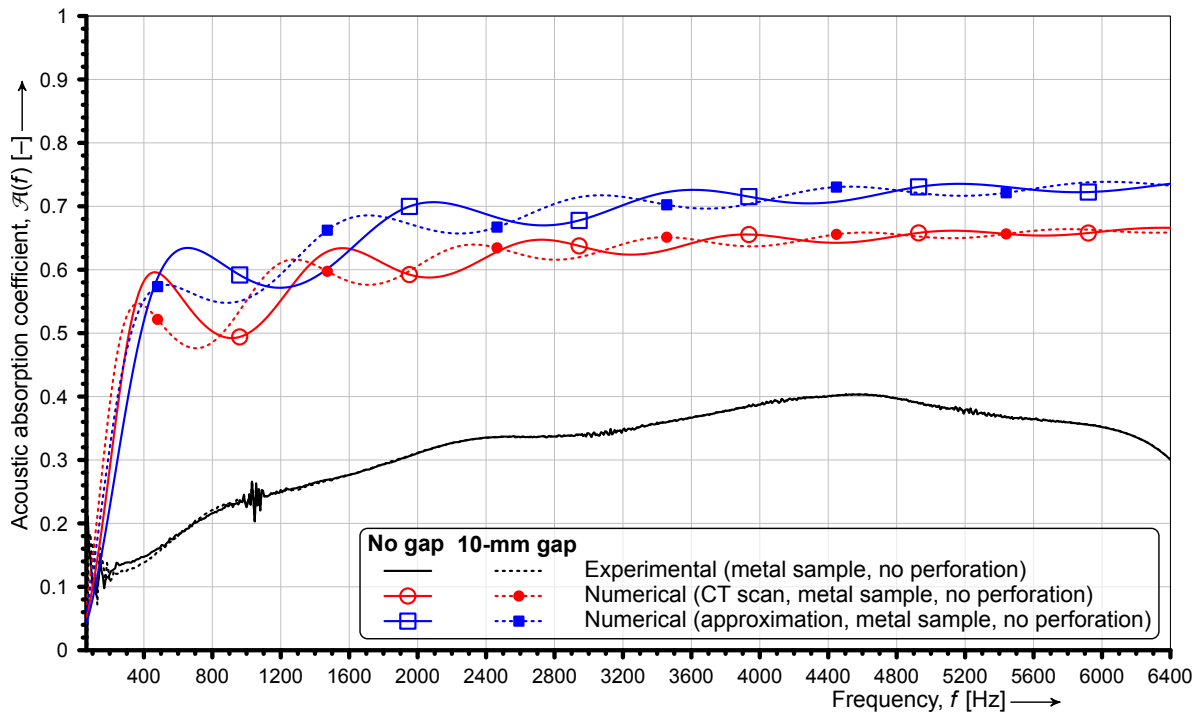
Figure 15: Numerical predictions (and experimental results) of the acoustic absorption coefficient for the foam without perforation based on the scanned (non-periodic) and approximate (periodic) unit cells.
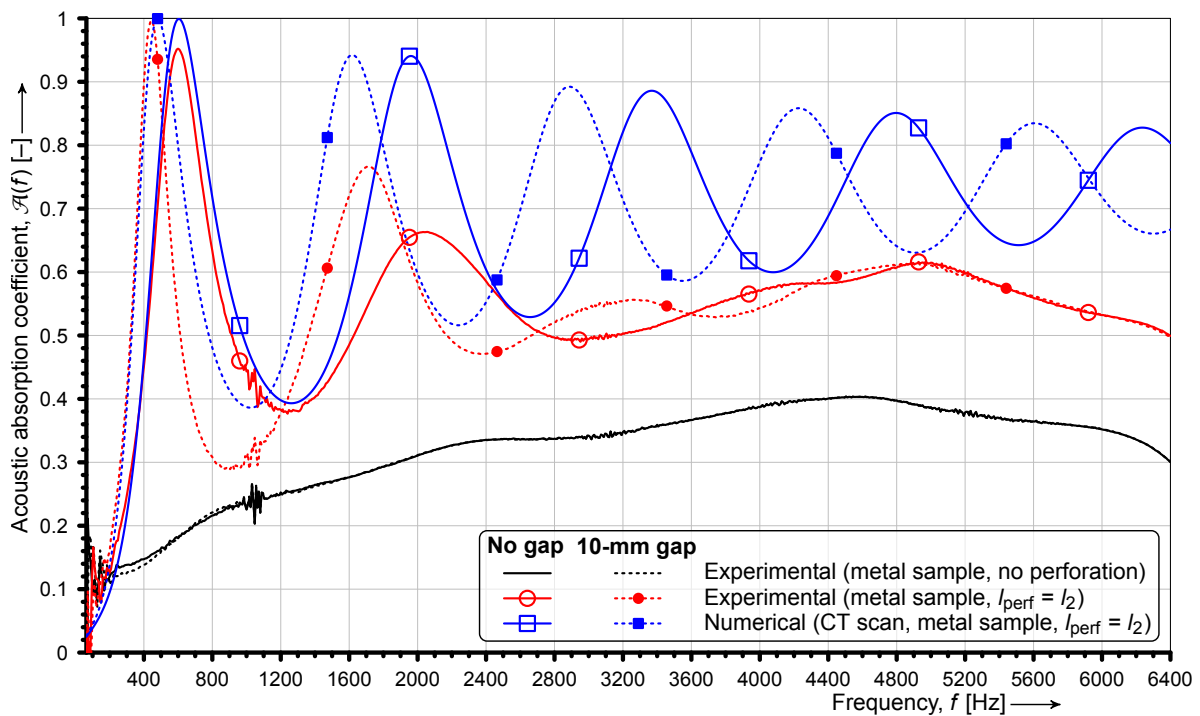

Figure 16: Numerical predictions (juxtaposed with experimental results) of the acoustic absorption coefficient for the foam with the second perforation pattern ($l_{\mathrm{perf}} = l_2$) based on the scanned (non-periodic) and approximate (periodic) unit cells.

resistivity is weaker than in the case of the real foam (Figure 15). However, the acoustic energy dissipation directly related to the absorption coefficient measured for the porous metal specimen perforated using the pattern with $l_{\mathrm{perf}} = l_3$ (and even with $l_{\mathrm{perf}} = l_2$) is fairly well estimated by means of the unit cells with cylindrical channels (see Figures 16 and 17). The visible discrepancies, in fact analogous to those observed for 3D printed porous materials (see [5, 6, 17, 18], for instance), essentially come from various reproduction as well as modelling imperfections, e.g. the utilisation of symmetry boundary conditions in the case of the scanned (non-periodic) microgeometries. They are influenced by many factors, including the selection of position at which the approximate (periodic) unit cell is virtually drilled (the presented results were achieved for the cell-centred perforation). Nevertheless, the frequencies and magnitudes of the first absorption peaks found for the perforated aluminium foam ($l_{\mathrm{perf}} = l_3$) with and without the air gap behind, were captured correctly by
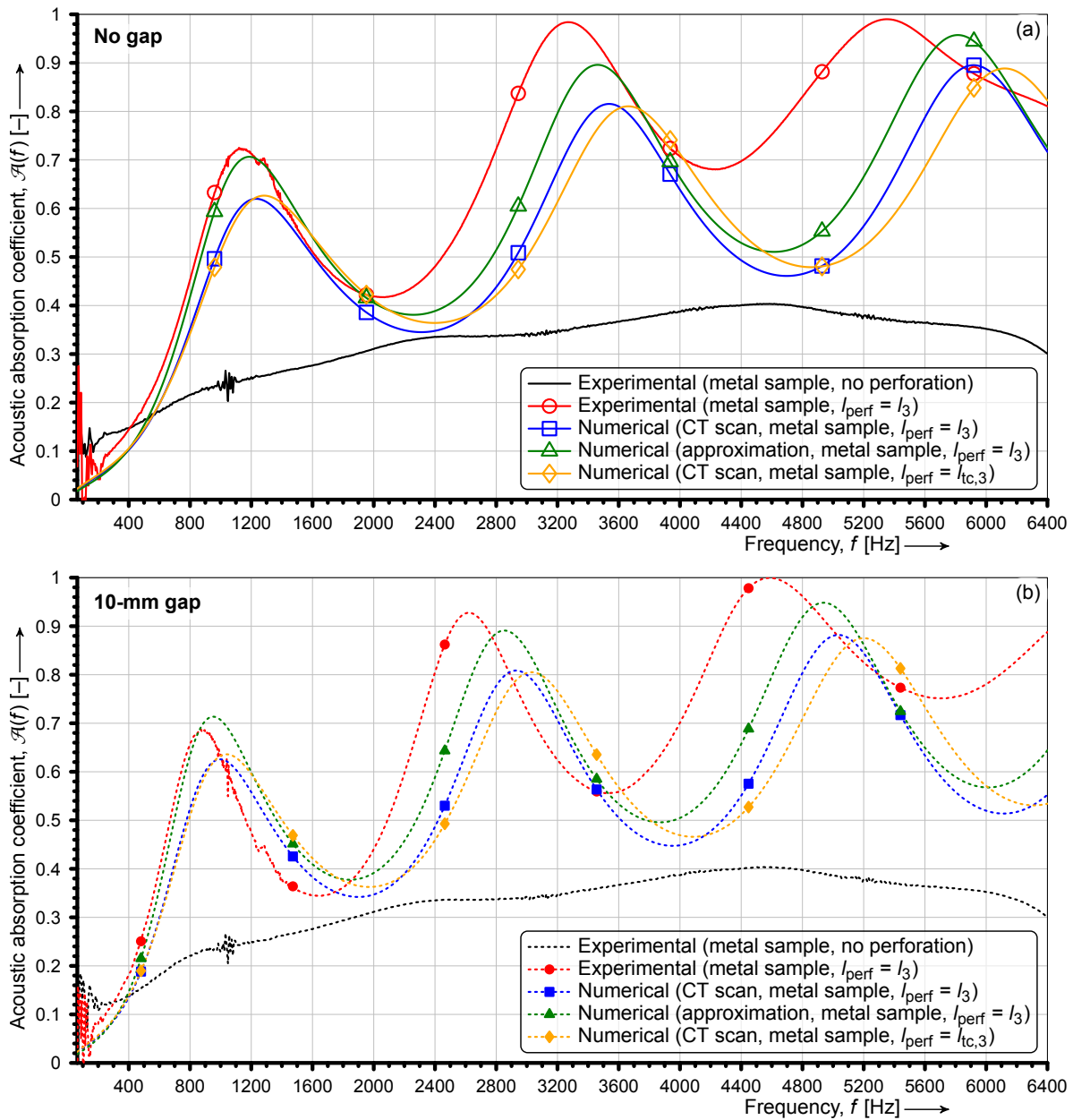
Figure 17: Experimental results and numerical predictions of the acoustic absorption coefficient for the foam with the third perforation pattern ($l_{\mathrm{perf}} = l_3$) based on the scanned (non-periodic) and approximate (periodic) unit cells: (a) without an air gap, and (b) with a 10-mm air gap between the material and rigid termination.

predictions based on the simplified structure with spherical pores (cf. Figure 17). Worth noting is also the fact, that the difference in topology between the third and fourth patterns (i.e. single- vs. two-channel perforation) does not affect much the sound absorption of a foam consisting of CT scanned cells as indicated by numerical calculations. The discrepancies between the two corresponding curves in Figure 17 are in general smaller than in the case of a perforated solid (as shown in Figure 13), which suggests that the application of the third perforation effectively opens the metal foam pore network being a principal domain of acoustic energy dissipation (the effect of the perforation itself is not dominant).

6   Final remarks

Drilling holes in a closed-cell aluminium foam (i.e. opening its porosity) is usually very profitable if one considers its acoustic application as a noise absorber. This paper delves into the aspects of modelling the propagation and attenuation of acoustic waves inside perforated metal foams that initially had (nearly) closed and irregular, albeit isotropic, pore network. The conducted analytical, numerical (finite element), and experimental analyses indicate that the perforated porous material is much better in sound absorption than its solid equivalent regardless of the investigated situation. In addition, it weighs less than a metal perforated plate of the same thickness and still can be successfully used in harsh conditions, e.g. on hot surfaces of an engine or turbine. The reported gain stems from the intensification of visco-inertial

and thermal losses occurring within newly opened and previously almost inaccessible fluid regions. The calculations yielding the presented observations were run on authentic (CT scanned) as well as largely simplified air domains. The real internal structure of the original foam was approximated by means of a random periodic arrangement of spherical pores. Despite such very simplified shapes, a fairy good agreement with both CT-based solutions and impedance tube measurements was reached. All in all, the accuracy of the predictions made is not perfect, but dependent on many factors like the selection of a representative unit cell, position of the perforation applied to it (viz. whether it is cell-centred or not), and the particular criteria (average pore diameter, window diameter between two linked pores, target number of pores, etc.) set during the generation of an approximative unit cell. Judging by the final results, the approach appears to work well for this sort of rigid porous media and supposedly can be effectively adapted to address other problems arising out of them.

The acoustic properties, and the sound absorption in particular, of any foam are influenced by many factors, although in the studied problem (airborne acoustic waves, rigid-frame media) they are related only to the microgeometry and not to the material of the skeleton. The only wave carrier is air in the pores, which means that the shape and characteristic sizes of the pore network play a key role in wave propagation.

One of the main parameters of the pore network affecting the propagation and absorption of acoustic waves is the open porosity. The original porosity of the examined aluminium foam is mostly closed, and therefore it is very important to open it to airborne acoustic waves. The proposed simple perforation patterns serve this purpose well. This makes the entire tortuous pore network of the foam accessible to the vibrations of air particles. In view of enlarged flow paths and thus reduced speed of sound, the tortuosity is another very important factor related to the propagation and absorption of acoustic waves in porous media. In fact, the high-frequency tortuosity and its dynamic visco-inertial and thermal generalisations are often involved in the advanced modelling of these phenomena. High tortuosity has a very beneficial effect on sound absorption. In the case of perforated solid panels, an increase in tortuosity can be achieved by inclining the perforation channels, but usually it is much better to have an inherently tortuous pore network, e.g. the one of the aluminium foam.

Tortuosity is related to permeability, which is another very important parameter that strongly influences the acoustic properties of porous materials. (Alternatively, the flow resistivity, which is inversely proportional to the permeability, is used.) In the advanced poro-acoustic modelling dynamic viscous and thermal generalisations of permeability are introduced. The permeability of soundproofing materials should not be high, because the airborne acoustic waves will be only weakly attenuated when passing through the material, nor too low because the waves will be mostly reflected. Hence, a denser perforation pattern of smaller diameter channels (possibly oblique), if technically feasible, should be a better choice for the investigated foam. Then, the tortuous pore network of the foam should be largely opened and the waves let into the material, slowed down, and (at least partially) attenuated instead of being reflected.

There are also two characteristic lengths that have significant influence on the acoustic properties of porous media: the viscous length (roughly related to the size of the windows connecting the pores) and the thermal length (roughly related to the size of the pores). Taking the Alulight foam as an example, it was observed that the applied perforations increase the value of the viscous characteristic length several times, while keeping the thermal characteristic length almost unchanged. Finally, there are additional factors linked to the local pore geometry and present in the material, such as sharp edges or the roughness of the interior walls, which intensify the viscous drag forces between the oscillating air particles and the solid skeleton, thus enhancing viscous dissipation effects.

Acknowledgements

A   Analytical modelling

The propagation of acoustic waves in rigid solids perforated with uniform cylindrical channels of diameter d_{perf} normal to the incident surface can be analytically expressed by the following approximations for the dynamic tortuosity functions, $\alpha_{\mathrm{A}}(\omega)$ and $\alpha'_{\mathrm{A}}(\omega)$:

$$\alpha_{\mathrm{A}}(\omega) = G^{-1}\left(\frac{d_{\mathrm{perf}}}{2}\sqrt{\frac{\omega \varrho_{\mathrm{air}}}{\mu_{\mathrm{air}}}}\right), \qquad \alpha'_{\mathrm{A}}(\omega) = G^{-1}\left(\frac{d_{\mathrm{perf}}}{2}\sqrt{N_{\mathrm{Pr,air}}\frac{\omega \varrho_{\mathrm{air}}}{\mu_{\mathrm{air}}}}\right), \tag{12}$$

where $G(\xi) \equiv 1 - 2J_1\left(\xi\sqrt{-i}\right)\left(\xi\sqrt{-i}\,J_0\left(\xi\sqrt{-i}\right)\right)^{-1}$ incorporates the Bessel functions of the first kind for integer orders 0 and 1, denoted as J_0 and J_1, respectively [63, 64]. To use the above formulae, one also needs to specify the dynamic viscosity, μ_{air}, Prandtl number, $N_{\text{Pr,air}}$, and density, ϱ_{air}, of the fluid (air in this case) saturating the open space inside the porous structure. Then, the equivalent properties of the considered medium are computed from Equation (2), and the sound absorption coefficient for a certain material layer, backed by an air cavity or not, is worked out using Equations (3)–(5).

B   Numerical modelling with the JCALP model

The macroscopic acoustic response of a rigid-frame porous material is often predicted by semi-phenomenological models. One of the most versatile of them is the Johnson-Champoux-Allard-Lafarge-Pride model [32, 65–70], where the dynamic tortuosities, $\alpha_{\text{N}}(\omega)$ and $\alpha'_{\text{N}}(\omega)$, called here "numerical", are defined employing eight "transport" parameters: the open porosity ϕ, (static) viscous permeability k_0, (static) thermal permeability k'_0, (high-frequency) tortuosity α_∞, static viscous tortuosity α_0, static thermal tortuosity α'_0, viscous characteristic length Λ, and thermal characteristic length Λ'. All of these intrinsic parameters can be evaluated on a (periodic, but not necessarily) unit cell representative for the porous microgeometry of a given medium either directly (in the case of ϕ and Λ') or using volume-averaging and the solutions to three steady-state boundary value problems posed on the fluid domain at the microscale level, namely:

1. an incompressible, viscous flow (known as the Stokes flow) driven by a unit pressure gradient parallel to the direction of acoustic wave propagation with the no-slip boundary condition set on solid walls—solved to determine k_0 and α_0;

2. an electric conduction problem in a pore-fluid caused by the application of a uniform, dimensionless, unit (electric) vector field in the direction of acoustic wave propagation with a dielectric skeleton and described by the Laplace equation—solved to determine α_∞ and Λ;

3. a thermal diffusion inside the fluid with the isothermal boundary condition imposed on solid surfaces, expressed through the Poisson equation—solved to determine k'_0 and α'_0.

For a more detailed discussion and necessary equations see, e.g. [2, 3, 19–22, 26, 71, 72]. When the required transport and fluid parameters are known, the following semi-phenomenological formulae of the JCALP model allow to calculate analytically the dynamic viscous tortuosity:

$$\alpha_{\text{N}}(\omega) = \alpha_\infty + \frac{\mu_{\text{air}}}{i\omega\varrho_{\text{air}}}\frac{\phi}{k_0}\left(\sqrt{\frac{i\omega\varrho_{\text{air}}}{\mu_{\text{air}}}\left(\frac{2\alpha_\infty k_0}{\Lambda\phi}\right)^2 + b^2} - b + 1\right), \qquad b = \frac{2\alpha_\infty{}^2 k_0}{\Lambda^2\phi(\alpha_0 - \alpha_\infty)}, \qquad (13)$$

and the dynamic thermal tortuosity:

$$\alpha'_{\text{N}}(\omega) = 1 + \frac{\mu_{\text{air}}}{i\omega\varrho_{\text{air}}N_{\text{Pr,air}}}\frac{\phi}{k'_0}\left(\sqrt{\frac{i\omega\varrho_{\text{air}}N_{\text{Pr,air}}}{\mu_{\text{air}}}\left(\frac{2k'_0}{\Lambda'\phi}\right)^2 + b'^2} - b' + 1\right), \qquad b' = \frac{2k'_0}{\Lambda'^2\phi(\alpha'_0 - 1)}. \qquad (14)$$

These functions are used to compute the equivalent material properties (2) necessary to evaluate the acoustic descriptors for a porous layer (or a multi-layer system), namely the surface acoustic impedance $Z_{\text{s}}(\omega)$ and the acoustic absorption coefficient $\mathcal{A}(\omega)$ according to Equations (3)–(5).

References

[1] C. Perrot, R. Panneton, X. Olny, Periodic unit cell reconstruction of porous media: Application to open-cell aluminum foams, J. Appl. Phys. 101 (2007) 113538. `doi:10.1063/1.2745095`.

[2] C. Perrot, F. Chevillotte, R. Panneton, Dynamic viscous permeability of an open-cell aluminum foam: Computations versus experiments, J. Appl. Phys. 103 (2008) 024909. `doi:10.1063/1.2829774`.

[3] F. Chevillotte, C. Perrot, R. Panneton, Microstructure based model for sound absorption predictions of perforated closed-cell metallic foams, J. Acoust. Soc. Am. 128 (2010) 1766–1776. `doi:10.1121/1.3473696`.

[4] T. G. Zieliński, Generation of random microstructures and prediction of sound velocity and absorption for open foams with spherical pores, J. Acoust. Soc. Am. 137 (2015) 1790–1801. `doi:10.1121/1.4915475`.

[5] K. C. Opiela, M. Rak, T. G. Zieliński, A concept demonstrator of adaptive sound absorber/insulator involving microstructure-based modelling and 3D printing, in: W. Desmet, B. Pluymers, D. Moens, W. Rottiers (Eds.), Proc. of ISMA2018 International Conference on Noise and Vibration Engineering/USD2018 International Conference on Uncertainty in Structural Dynamics, KU Leuven, Belgium, 2018, pp. 1091–1104.

[6] K. C. Opiela, T. G. Zieliński, Microstructural design, manufacturing and dual-scale modelling of an adaptable porous composite sound absorber, Compos. Part B-Eng. 187 (2020) 107833. `doi:10.1016/j.compositesb.2020.107833`.

[7] C. Perrot, F. Chevillotte, M. T. Hoang, G. Bonnet, F.-X. Bécot, L. Gautron, A. Duval, Microstructure, transport, and acoustic properties of open-cell foam samples: Experiments and three-dimensional numerical simulations, J. Appl. Phys. 111 (2012) 014911. `doi:10.1063/1.3673523`.

[8] O. Doutres, M. Ouisse, N. Atalla, M. Ichchou, Impact of the irregular microgeometry of polyurethane foam on the macroscopic acoustic behavior predicted by a unit-cell model, J. Acoust. Soc. Am. 136 (2014) 1666–1681. doi:10.1121/1.4895695.

[9] J. H. Park, K. S. Minn, H. R. Lee, S. H. Yang, C. B. Yu, S. Y. Pak, C. S. Oh, Y. S. Song, Y. J. Kang, J. R. Youn, Cell openness manipulation of low density polyurethane foam for efficient sound absorption, J. Sound Vib. 406 (2017) 224–236. doi:10.1016/j.jsv.2017.06.021.

[10] J. H. Park, S. H. Yang, H. R. Lee, C. B. Yu, S. Y. Pak, C. S. Oh, Y. J. Kang, J. R. Youn, Optimization of low frequency sound absorption by cell size control and multiscale poroacoustics modeling, J. Sound Vib. 397 (2017) 17–30. doi:10.1016/j.jsv.2017.03.004.

[11] K. Gao, J. A. W. van Dommelen, M. G. D. Geers, Investigation of the effects of the microstructure on the sound absorption performance of polymer foams using a computational homogenization approach, Eur. J. Mech. A-Solid. 61 (2017) 330–344. doi:10.1016/j.euromechsol.2016.10.011.

[12] M. J. Cops, J. G. McDaniel, E. A. Magliula, D. J. Bamford, J. Bliefnick, Measurement and analysis of sound absorption by a composite foam, Appl. Acoust. 160 (2020) 107138. doi:10.1016/j.apacoust.2019.107138.

[13] F. Chevillotte, C. Perrot, E. Guillon, A direct link between microstructure and acoustical macro-behavior of real double porosity foams, J. Acoust. Soc. Am. 134 (2013) 4681–4690. doi:10.1121/1.4824842.

[14] V.-H. Nguyen, E. Rohan, S. Naili, Multiscale simulation of acoustic waves in homogenized heterogeneous porous media with low and high permeability contrasts, Int. J. Eng. Sci. 101 (2016) 92–109. doi:doi.org/10.1016/j.ijengsci.2015.12.004.

[15] K. Gao, J. A. W. van Dommelen, M. G. D. Geers, Microstructure characterization and homogenization of acoustic polyurethane foams: Measurements and simulations, Int. J. Solids Struct. 100–101 (2016) 536–546. doi:10.1016/j.ijsolstr.2016.09.024.

[16] J. Park, S. H. Yang, K. S. Minn, C. B. Yu, S. Y. Pak, Y. S. Song, J. R. Youn, Design and numerical analysis of syntactic hybrid foam for superior sound absorption, Mater. Design 142 (2018) 212–220. doi:10.1016/j.matdes.2018.01.040.

[17] T. G. Zieliński, Pore-size effects in sound absorbing foams with periodic microstructure: Modelling and experimental verification using 3D printed specimens, in: P. Sas, D. Moens, A. van de Walle (Eds.), Proc. of ISMA2016 International Conference on Noise and Vibration Engineering/USD2016 International Conference on Uncertainty in Structural Dynamics, KU Leuven, Belgium, 2016, pp. 95–104.

[18] K. C. Opiela, T. G. Zieliński, Adaptation of the equivalent-fluid model to the additively manufactured acoustic porous materials, in: M. Ochmann, M. Vorländer, J. Fels (Eds.), Proc. of the 23rd International Congress on Acoustics: Integrating 4th EAA Euroregio 2019, Deutsche Gesellschaft für Akustik, Berlin, Germany, 2019, pp. 1216–1223.

[19] S. Gasser, F. Paun, Y. Bréchet, Absorptive properties of rigid porous media: Application to face centered cubic sphere packing, J. Acoust. Soc. Am. 117 (2005) 2090–2099. doi:10.1121/1.1863052.

[20] C.-Y. Lee, M. J. Leamy, J. H. Nadler, Acoustic absorption calculation in irreducible porous media: A unified computational approach, J. Acoust. Soc. Am. 126 (2009) 1862–1870. doi:10.1121/1.3205399.

[21] T. G. Zieliński, Microstructure-based calculations and experimental results for sound absorbing porous layers of randomly packed rigid spherical beads, J. Appl. Phys. 116 (2014) 034905. doi:10.1063/1.4890218.

[22] C. Perrot, F. Chevillotte, R. Panneton, Bottom-up approach for microstructure optimization of sound absorbing materials, J. Acoust. Soc. Am. 124 (2008) 940–948. doi:10.1121/1.2945115.

[23] T. G. Zieliński, Microstructure representations for sound absorbing fibrous media: 3D and 2D multiscale modelling and experiments, J. Sound Vib. 409 (2017) 112–130. doi:10.1016/j.jsv.2017.07.047.

[24] S. Ren, F. Xin, T. J. Lu, C. Zhang, A semi-analytical model for the influence of temperature on sound propagation in sintered metal fiber materials, Mater. Design 134 (2017) 513–522. doi:10.1016/j.matdes.2017.09.007.

[25] K. Attenborough, Macro- and micro-structure designs for porous sound absorbers, Appl. Acoust. 145 (2019) 349–357. doi:10.1016/j.apacoust.2018.10.018.

[26] T. G. Zieliński, F. Chevillotte, E. Deckers, Sound absorption of plates with micro-slits backed with air cavities: Analytical estimations, numerical calculations and experimental validations, Appl. Acoust. 146 (2019) 261–279. doi:10.1016/j.apacoust.2018.11.026.

[27] A. E. Tiuc, O. Nemeş, H. Vermeşan, A. C. Toma, New sound absorbent composite materials based on sawdust and polyurethane foam, Compos. Part B-Eng. 165 (2019) 120–130. doi:10.1016/j.compositesb.2018.11.103.

[28] Y. Yang, B. Li, Z. Chen, N. Sui, Z. Chen, M.-U. Saeed, Y. Li, R. Fu, C. Wu, Y. Jing, Acoustic properties of glass fiber assembly-filled honeycomb sandwich panels, Compos. Part B-Eng. 96 (2016) 281–286. doi:10.1016/j.compositesb.2016.04.046.

[29] C. Lagarrigue, J.-P. Groby, O. Dazel, V. Tournat, Design of metaporous supercells by genetic algorithm for absorption optimization on a wide frequency band, Appl. Acoust. 102 (2016) 49–54. doi:10.1016/j.apacoust.2015.09.011.

[30] J.-P. Groby, C. Lagarrigue, B. Brouard, O. Dazel, V. Tournat, B. Nennig, Using simple shape three-dimensional rigid inclusions to enhance porous layer absorption, J. Acoust. Soc. Am. 136 (2014) 1139–1148. doi:10.1121/1.4892760.

[31] T. G. Zieliński, Numerical investigation of active porous composites with enhanced acoustic absorption, J. Sound Vib. 330 (2011) 5292–5308. doi:10.1016/j.jsv.2011.05.029.

[32] J.-F. Allard, N. Atalla, Propagation of sound in porous media: Modelling sound absorbing materials, 2nd Edition, John Wiley & Sons, 2009. doi:10.1002/9780470747339.

[33] P. De Jaeger, C. T'Joen, H. Huisseune, B. Ameel, M. De Paepe, An experimentally validated and parameterized periodic unit-cell reconstruction of open-cell foams, J. Appl. Phys. 109 (2011) 103519. doi:10.1063/1.3587159.

[34] C. Perrot, X. Olny, R. Panneton, R. Bouchard, Computation of the dynamic thermal properties of a three-dimensional unit cell of porous media by Brownian motion simulation, J. Acoust. Soc. Am. 115 (2004) 2625–2625. doi:10.1121/1.4784836.

[35] C. Perrot, R. Panneton, X. Olny, Linking microstructure and acoustic properties of open-cell foams, J. Acoust. Soc. Am. 120 (2006) 3145–3145. doi:10.1121/1.4787789.

[36] A. J. Otaru, Enhancing the sound absorption performance of porous metals using tomography images, Appl. Acoust. 143 (2019) 183–189. doi:doi.org/10.1016/j.apacoust.2018.09.007.

[37] D. Guan, J. H. Wu, J. Wu, J. Li, W. Zhao, Acoustic performance of aluminum foams with semiopen cells, Appl. Acoust. 87 (2015) 103–108. doi:10.1016/j.apacoust.2014.06.016.

[38] T. J. Lu, F. Chen, D. He, Sound absorption of cellular metals with semiopen cells, J. Acoust. Soc. Am. 108 (2000) 1697–1709. `doi:10.1121/1.1286812`.

[39] N. Atalla, R. Panneton, F. C. Sgard, X. Olny, Acoustic absorption of macro-perforated porous materials, J. Sound Vib. 243 (2001) 659–678. `doi:10.1006/jsvi.2000.3435`.

[40] F. C. Sgard, X. Olny, N. Atalla, F. Castel, On the use of perforations to improve the sound absorption of porous materials, Appl. Acoust. 66 (2005) 625–651. `doi:10.1016/j.apacoust.2004.09.008`.

[41] M. A. Navacerrada, P. Fernández, C. Díaz, A. Pedrero, Thermal and acoustic properties of aluminium foams manufactured by the infiltration process, Appl. Acoust. 74 (2013) 496–501. `doi:10.1016/j.apacoust.2012.10.006`.

[42] H. Yu, G. Yao, X. Wang, Y. Liu, H. Li, Sound insulation property of Al-Si closed-cell aluminum foam sandwich panels, Appl. Acoust. 68 (2007) 1502–1510. `doi:10.1016/j.apacoust.2006.07.019`.

[43] M. F. Ashby, A. G. Evans, N. A. Fleck, L. J. Gibson, J. W. Hutchinson, H. N. G. Wadley (Eds.), Metal foams: A design guide, 1st Edition, Butterworth-Heinemann, Burlington, 2000. `doi:10.1016/B978-075067219-1/50004-0`.

[44] O. Doutres, N. Atalla, M. Brouillette, C. Hébert, Using shock waves to improve the sound absorbing efficiency of closed-cell foams, Appl. Acoust. 79 (2014) 110–116. `doi:10.1016/j.apacoust.2013.12.022`.

[45] T. J. Lu, A. Hess, M. F. Ashby, Sound absorption in metallic foams, J. Appl. Phys. 85 (1999) 7528–7539. `doi:10.1063/1.370550`.

[46] T. Miyoshi, M. Itoh, S. Akiyama, A. Kitahara, ALPORAS aluminum foam: Production process, properties, and applications, Adv. Eng. Mater. 2 (2000) 179–183. `doi:10.1002/(SICI)1527-2648(200004)2:4<179::AID-ADEM179>3.0.CO;2-G`.

[47] A. Ghazi, P. Berke, K. Ehab Moustafa Kamel, B. Sonon, C. Tiago, T. J. Massart, Multiscale computational modelling of closed cell metallic foams with detailed microstructural morphological control, Int. J. Eng. Sci. 143 (2019) 92–114. `doi:10.1016/j.ijengsci.2019.06.012`.

[48] A. Adamčíková, B. Taraba, J. Kováčik, A study of porosity influence on thermal diffusivity of aluminium foam by experimental analysis and numerical simulation, in: A. Öchsner, G. E. Murch, A. Shokuhfar, J. M. P. Q. Delgado (Eds.), Diffusion in Solids and Liquids V, Vol. 297 of Defect and Diffusion Forum, Trans Tech Publications Ltd, 2010, pp. 814–819. `doi:10.4028/www.scientific.net/DDF.297-301.814`.

[49] J. Kováčik, F. Simančík, Aluminium foam—Modulus of elasticity and electrical conductivity according to percolation theory, Scripta Mater. 39 (1998) 239–246. `doi:10.1016/S1359-6462(98)00151-1`.

[50] J. Kováčik, Ľ. Orovčík, J. Jerz, High-temperature compression of closed cell aluminium foams, Kovové Mater. 54 (2016) 429–440. `doi:10.4149/km-2016-6-429`.

[51] J. Kováčik, J. Jerz, N. Mináriková, L. Marsavina, E. Linul, Scaling of compression strength in disordered solids: Metallic foams, Frattura Integr. Strutt. 36 (2016) 55–62. `doi:10.3221/IGF-ESIS.36.06`.

[52] J. Kováčik, L. Marsavina, E. Linul, Poisson's ratio of closed-cell aluminium foams, Materials 11 (2018) 1904. `doi:10.3390/ma11101904`.

[53] E. Linul, L. Marsavina, J. Kováčik, Collapse mechanisms of metal foam matrix composites under static and dynamic loading conditions, Mat. Sci. Eng. A-Struct. 690 (2017) 214–224. `doi:10.1016/j.msea.2017.03.009`.

[54] M. Nosko, F. Simančík, R. Florek, Reproducibility of aluminum foam properties: Effect of precursor distribution on the structural anisotropy and the collapse stress and its dispersion, Mat. Sci. Eng. A-Struct. 527 (2010) 5900–5908. `doi:10.1016/j.msea.2010.05.073`.

[55] Ľ. Orovčík, M. Nosko, J. Kováčik, T. Dvorák, M. Štěpánek, F. Simančík, Effects of chemical composition on the pore structure and heat treatment on the deformation of PM aluminium foams 6061 and 7075, Kovové Mater. 54 (2016) 463–470. `doi:10.4149/km_2016_6_463`.

[56] I. Sevostianov, J. Kováik, F. Simaník, Correlation between elastic and electric properties for metal foams: Theory and experiment, Int. J. Fracture 114 (2002) 23–28. `doi:10.1023/A:1022674130262`.

[57] I. Sevostianov, J. Kováčik, F. Simančík, Elastic and electric properties of closed-cell aluminum foams: Cross-property connection, Mat. Sci. Eng. A-Struct. 420 (2006) 87–99. `doi:10.1016/j.msea.2006.01.064`.

[58] M. Nosko, F. Simančík, K. Iždinský, P. Švec, R. Florek, Stabilizing intermetallic phases within aluminum foam, Mater. Lett. 65 (2011) 1378–1380. `doi:10.1016/j.matlet.2011.02.007`.

[59] T. D. Ngo, A. Kashani, G. Imbalzano, K. T. Q. Nguyen, D. Hui, Additive manufacturing (3D printing): A review of materials, methods, applications and challenges, Compos. Part B-Eng. 143 (2018) 172–196. `doi:10.1016/j.compositesb.2018.02.012`.

[60] ISO 10534-2, Acoustics — Determination of sound absorption coefficient and impedance in impedance tubes — Part 2: Transfer-function method, ISO standard, International Organisation for Standardization, Case postale 56, CH-1211 Genève 20, Switzerland (Nov. 1998).

[61] T. G. Zieliński, K. C. Opiela, P. Pawłowski, N. Dauchez, T. Boutin, J. Kennedy, D. Trimble, H. Rice, B. Van Damme, G. Hannema, R. Wróbel, S. Kim, S. G. Mosanenzadeh, N. X. Fang, J. Yang, B. Briere de la Hosseraye, M. C. J. Hornikx, E. Salze, M.-A. Galland, R. Boonen, A. Carvalho de Sousa, E. Deckers, M. Gaborit, J.-P. Groby, Reproducibility of sound-absorbing periodic porous materials using additive manufacturing technologies: Round robin study, Addit. Manuf. 36 (2020) 101564. `doi:10.1016/j.addma.2020.101564`.

[62] T. J. Cox, P. D'Antonio, Acoustic absorbers and diffusers: Theory, design and application, Taylor & Francis, 2004.

[63] K. Attenborough, Microstructures for lowering the quarter wavelength resonance frequency of a hard-backed rigid-porous layer, Appl. Acoust. 130 (2018) 188–194. `doi:10.1016/j.apacoust.2017.09.022`.

[64] M. R. Stinson, The propagation of plane sound waves in narrow and wide circular tubes, and generalization to uniform tubes of arbitrary cross-sectional shape, J. Acoust. Soc. Am. 89 (1991) 550–558. `doi:10.1121/1.400379`.

[65] D. L. Johnson, J. Koplik, R. Dashen, Theory of dynamic permeability and tortuosity in fluid-saturated porous media, J. Fluid Mech. 176 (1987) 379–402. `doi:10.1017/S0022112087000727`.

[66] Y. Champoux, J.-F. Allard, Dynamic tortuosity and bulk modulus in air-saturated porous media, J. Appl. Phys. 70 (1991) 1975–1979. `doi:doi.org/10.1063/1.349482`.

[67] S. R. Pride, A. F. Gangi, F. D. Morgan, Deriving the equations of motion for porous isotropic media, J. Acoust. Soc. Am. 92 (1992) 3278–3290. `doi:10.1121/1.404178`.

[68] S. R. Pride, F. D. Morgan, A. F. Gangi, Drag forces of porous-medium acoustics, Phys. Rev. B 47 (1993) 4964–4978. `doi:10.1103/PhysRevB.47.4964`.

[69] D. Lafarge, Comments on "Rigorous link between fluid permeability, electric conductivity, and relaxation times for transport in porous media", Phys. Fluids A-Fluid 5 (1993) 500–502. `doi:10.1063/1.858873`.

[70] D. Lafarge, P. Lemarinier, J.-F. Allard, V. Tarnow, Dynamic compressibility of air in porous structures at audible frequencies, J. Acoust. Soc. Am. 102 (1997) 1995–2006. `doi:10.1121/1.419690`.

[71] T. G. Zieliński, R. Venegas, C. Perrot, M. Červenka, F. Chevillotte, K. Attenborough, Benchmarks for microstructure-based modelling of sound absorbing rigid-frame porous media, J. Sound Vib. 483 (2020) 115441. `doi:10.1016/j.jsv.2020.115441`.

[72] M. Firdaouss, J.-L. Guermond, D. Lafarge, Some remarks on the acoustic parameters of sharp-edged porous media, Int. J. Eng. Sci. 36 (1998) 1035–1046. `doi:10.1016/S0020-7225(98)00002-0`.

[73] M. S. Alnæs, J. Blechta, J. Hake, A. Johansson, B. Kehlet, A. Logg, C. Richardson, J. Ring, M. E. Rognes, G. N. Wells, The FEniCS Project version 1.5, Arch. Num. Soft. 3 (2015) 9–23. `doi:10.11588/ans.2015.100.20553`.

[74] O. C. Zienkiewicz, R. L. Taylor, J. Z. Zhu, The finite element method: Its basis and fundamentals, 7th Edition, Butterworth-Heinemann, 2013. `doi:10.1016/B978-1-85617-633-0.00019-8`.

[75] P. Leclaire, O. Umnova, T. Dupont, R. Panneton, Acoustical properties of air-saturated porous material with periodically distributed dead-end pores, J. Acoust. Soc. Am. 137 (2015) 1772–1782. `doi:10.1121/1.4916712`.

[76] O. Dazel, F. Sgard, F.-X. Bécot, N. Atalla, Expressions of dissipated powers and stored energies in poroelastic media modeled by {u,U} and {u,P} formulations, J. Acoust. Soc. Am. 123 (2008) 2054–2063. `doi:10.1121/1.2874520`.